Draft version January 23, 2022
Typeset using LaTeX **twocolumn** style in AASTeX63

arXiv:2002.09826v3 [astro-ph.CO] 9 Nov 2020

Unveiling the Intrinsic Alignment of Galaxies with Self-Calibration and DECaLS DR3 data

Ji Yao [1], Huanyuan Shan [2], Pengjie Zhang [1,3,4], Jean-Paul Kneib [5,6] and Eric Jullo [6]

[1] *Department of Astronomy, Shanghai Jiao Tong University, Shanghai 200240, China*
[2] *Shanghai Astronomical Observatory (SHAO), Nandan Road 80, Shanghai 200030, China*
[3] *Tsung-Dao Lee Institute, Shanghai Jiao Tong University, Shanghai 200240, China*
[4] *Shanghai Key Laboratory for Particle Physics and Cosmology, China*
[5] *Institute of Physics, Laboratory of Astrophysics, Ecole Polytechnique Fédérale de Lausanne (EPFL), Observatoire de Sauverny, 1290 Versoix, Switzerland*
[6] *Aix-Marseille Univ, CNRS, CNES, LAM, Marseille, France*

Submitted to ApJ

ABSTRACT

Galaxy intrinsic alignment (IA) is both a source of systematic contamination to cosmic shear measurement and its cosmological applications, and a source of valuable information on the large scale structure of the universe and galaxy formation. The self-calibration (SC) method (Zhang 2010a) was designed to separate IA from cosmic shear, free of IA modeling. It was first successfully applied to the KiDS450 and KV450 data (Yao et al. 2020). We improved the SC method in several aspects, and apply it to the DECaLS DR3 shear + photo-z catalog and significantly improve the IA detection to $\sim 14\sigma$. We find a strong dependence of IA on galaxy color, with strong IA signal ($\sim 17.6\sigma$) for red galaxies, while the IA signal for blue galaxies is consistent with zero. The detected IA for red galaxies are in reasonable agreement with the non-linear tidal alignment model and the inferred IA amplitude increases with redshift. Our measurements rule out the constant IA amplitude assumption at $\sim 3.9\sigma$ for the red sample. We address the systematics in the SC method carefully and performed several sanity checks. We discuss various caveats such as redshift/shear calibrations and possible improvements in the measurement, theory and parameter fitting that will be addressed in future works.

Keywords: cosmology, gravitational lensing: weak, observations, large-scale structure of the universe, galaxy

1. INTRODUCTION

For many cosmological probes, systematic errors in either observation or theory or both are becoming the dominant source of errors. They may already be responsible for several tensions in cosmology, such as the H_0 tension (Riess et al. 2019; Planck Collaboration et al. 2020; Bernal et al. 2016; Lin et al. 2019; Freedman et al. 2019). Another example is the $S_8 = \sigma_8(\Omega_m/0.3)^{\alpha\sim0.5}$ tension, between the Planck CMB experiment (Planck Collaboration et al. 2020) and the stage III weak lensing surveys such as KiDS (Kilo Degree Survey, Hildebrandt et al. (2017, 2020a); Asgari et al. (2020)), HSC (Hyper Suprime-Cam, Hamana et al. (2020); Hikage et al. (2019)), and DES (Dark Energy Survey, Troxel et al. (2018a)), with the S_8 differences varies in between $\sim 3\sigma$ and $\sim 1\sigma$. A variety of tests have been carried out in investigating the S_8 tension (e.g. Asgari et al. (2019); Troxel et al. (2018b); Chang et al. (2019); Joudaki et al. (2020)).

Among systematic errors in weak lensing cosmology based on cosmic shear measurement, the galaxy intrinsic alignment (IA) is a prominent one. Cosmic shear is extracted from galaxy shapes, with the underlying assumption that the intrinsic galaxy shapes have no spatial correlation. However, this assumption is invalid, since the large scale structure environment induces spatial correlation in the galaxy shapes. In the context of weak lensing, the spatially correlated part in the galaxy shapes (ellipticities) is called IA. It has been predicted

Corresponding author: Ji Yao, Huanyuan Shan, Pengjie Zhang
ji.yao@outlook.com; hyshan@shao.ac.cn; zhangpj@sjtu.edu.cn

by theory/simulations (e.g. Croft & Metzler (2000); Catelan et al. (2001); Crittenden et al. (2001); Jing (2002); Hirata & Seljak (2004); Joachimi et al. (2013); Kiessling et al. (2015); Blazek et al. (2015, 2019); Chisari et al. (2017); Xia et al. (2017)), and detected in observations (e.g. Lee & Pen (2001); Heymans et al. (2004); Bridle & King (2007); Okumura et al. (2009); Dossett & Ishak (2013); Rong et al. (2015); Krause et al. (2016); Kirk et al. (2015); Troxel et al. (2018a); Samuroff et al. (2019); Yao et al. (2020). It is one of the key limiting factors to fully realize the power of weak lensing cosmology (Heavens 2002; Refregier 2003; Hoekstra & Jain 2008; LSST Science Collaboration et al. 2009; Weinberg et al. 2013; Troxel & Ishak 2015; Joachimi et al. 2015; Kilbinger 2015; Mandelbaum 2018).

In cosmic shear data analysis, IA is often mitigated by fitting against an assumed fiducial IA template (Troxel et al. 2018a; Hildebrandt et al. 2017, 2020a; Hamana et al. 2020; Hikage et al. 2019). In contrast, the Self-Calibration (SC) methods (Zhang 2010a,b) were designed to remove the IA contamination without assumption on the IA model. This model independence is achieved, due to an intrinsic difference between the weak lensing field and the intrinsic alignment field. The former is a 2D (projected) field with a profound source-lens asymmetry, while the later is a statistically isotropic 3D field. The SC2008 method (Zhang 2010a) has been applied to stage IV survey forecasts (Yao et al. 2017, 2019), while the SC2010 method Zhang (2010b) has been examined in simulation (Meng et al. 2018) and combined with SC2008 in the forecast (Yao et al. 2019). These studies showed that the SC method is generally accurate in IA removal/measurement.

Yao et al. (2020) first applied the SC2008 method to KiDS450 (Hildebrandt et al. 2017) and KV450 (Hildebrandt et al. 2020a) shear catalogs. To implement the SC method and to incorporate with various observational effects such as photo-z errors, Yao et al. (2020) built a Lensing-IA Separation (LIS) pipeline, and succeeded in the IA detection. To further test the applicability of the SC method, and to improve the IA detection and applications, we apply the same LIS pipeline to the DECaLS (Dark Energy Camera Legacy Survey) DR3 shear catalog (Phriksee et al. 2020). Comparing to the previous work, we have significantly more galaxies and larger sky coverage. We use the photo-z obtained from k-nearest-neighbours (Zou et al. 2019). These improvements result in more significant IA detection, and allow us to reveal more detailed information on IA such as its redshift and color dependence.

This paper is organized as follows. In §2, we briefly describe the SC method and the LIS pipeline. We also describe the theoretical model to compare with. §3 describes the DECalS DR3 data used for the analysis. §4 presents the main results and §5 discusses further implications and possible caveats. We include more technical details in the appendix.

2. THE SC METHOD AND THE LIS PIPELINE

The observed galaxy shape $\gamma^{\rm obs}$ contains three components,

$$\gamma^{\rm obs} = \gamma^G + \gamma^N + \gamma^I \ . \tag{1}$$

Here the superscript "G" denotes gravitational (G) lensing. The galaxy shape noise has a spatially uncorrelated part which we denote with the superscript "N", and a spatially correlated part (the intrinsic alignment) which we denote with the superscript "I". When cross-correlating $\gamma^{\rm obs}$ with galaxy number density δ_g, the γ^N term has no contribution. The measured correlation will contain two parts,

$$\langle \gamma^{\rm obs} \delta_g \rangle \ = \ \langle \gamma^G \delta_g \rangle + \langle \gamma^I \delta_g \rangle \ . \tag{2}$$

The first term on the right-hand side of the equation is the (lensing part) Gg correlation, and the second term is the (IA part) Ig correlation. The first step of SC2008 is to separate and measure Ig (and Gg), without resorting to IA modeling. The second step is to convert Ig into the GI term contaminating the measurement of cosmic shear auto-correlation, through a scaling relation found in Zhang (2010a). The current paper is restricted to the first step, since no results on the cosmic shear auto-correlation will be presented here. We focus on the Ig measurement and its application.

2.1. *Separating Gg and Ig*

For a pair of galaxies, we denote the photo-z of the galaxy used for shape measurement as z^P_γ, and the photo-z of the galaxy used for number density measurement as z^P_g. Both the intrinsic alignment and the galaxy number density fields are statistically isotropic 3D fields. Therefore the $\langle Ig \rangle$ correlation with $z^P_\gamma < z^P_g$ is identical to $\langle Ig \rangle$ with $z^P_\gamma > z^P_g$. Namely, it is insensitive to the ordering of (z^P_γ, z^P_g) pair in redshift space. This holds for both real (spectroscopic) redshift and photometric redshift. In contrast, the lensing correlation requires $z_\gamma > z_g$ for the true redshift (z). Therefore in the photo-z (z^P) space, the $\langle Gg \rangle$ correlation is smaller for the pairs with $z^P_\gamma < z^P_g$, compared with the $z^P_\gamma > z^P_g$ pairs.[1]

[1] In the limit of negligible photo-z error, the $\langle Gg \rangle$ correlation vanishes for $z^P_\gamma < z^P_g$ pairs. In reality, photo-z has both scatters and outliers, the $\langle Gg \rangle$ correlation persists even for $z^P_\gamma < z^P_g$ pairs.

Therefore we can form two sets of two-point statistics measured from the same data in the same photo-z bin (e.g. the *i-th* photo-z bin). In terms of the angular power spectrum,

$$C_{ii}^{\gamma g} = C_{ii}^{Gg} + C_{ii}^{Ig}, \tag{3a}$$
$$C_{ii}^{\gamma g}|_S = C_{ii}^{Gg}|_S + C_{ii}^{Ig} \ . \tag{3b}$$

Here $C_{ii}^{\gamma g}$ is the galaxy shape-number density angular power spectrum for all pairs in the i-th redshift bin, while $C_{ii}^{\gamma g}|_S$ is the one only for pairs with $z_\gamma^P < z_g^P$. According to the above analysis, with this "$|_S$" selection, the lensing signal drops from C_{ii}^{Gg} to $C_{ii}^{Gg}|_S$, while the IA signal C_{ii}^{Ig} remains the same.

The drop in the lensing signal can be determined by the Q parameter,

$$Q_i(\ell) \equiv \frac{C_{ii}^{Gg}|_S(\ell)}{C_{ii}^{Gg}(\ell)} \ . \tag{4}$$

$Q(\ell)$ has only weak dependence on cosmology and ℓ (Zhang 2010a; Yao et al. 2017). This makes the SC method cosmology-independent to good accuracy. But it is sensitive to the photo-z quality. $Q = 0$ for perfect photo-z (photo-z is accurate so that lensing signal drops fully due to the selection), $Q \to 1$ for poor photo-z, and $Q \in (0, 1)$ in general. We are then able to separate Gg and Ig (Zhang 2010a; Yao et al. 2020),

$$C_{ii}^{Gg}(\ell) = \frac{C_{ii}^{\gamma g}(\ell) - C_{ii}^{\gamma g}|_S(\ell)}{1 - Q_i(\ell)}, \tag{5}$$
$$C_{ii}^{Ig}(\ell) = \frac{C_{ii}^{\gamma g}|_S(\ell) - Q_i(\ell) C_{ii}^{\gamma g}(\ell)}{1 - Q_i(\ell)}. \tag{6}$$

In this work, we extended the formalism of SC to the correlation function, considering two additional effects comparing to previous works Zhang (2010a); Yao et al. (2017, 2020): (1) the scale-dependent $Q_i(\theta)$ and (2) impact from non-symmetric redshift distribution, leading to $w_{ii}^{Ig}|_S \neq w_{ii}^{Ig}$, or $C_{ii}^{Ig}|_S \neq C_{ii}^{Ig}$. As a result, we have

$$w_{ii}^{\gamma g}(\theta) = w_{ii}^{Gg}(\theta) + w_{ii}^{Ig}(\theta), \tag{7a}$$
$$w_{ii}^{\gamma g}|_S(\theta) = w_{ii}^{Gg}|_S(\theta) + w_{ii}^{Ig}|_S(\theta) \ , \tag{7b}$$

which give us

$$w_{ii}^{Gg}(\theta) = \frac{Q_i^{Ig}(\theta) w_{ii}^{\gamma g}(\theta) - w_{ii}^{\gamma g}|_S(\theta)}{Q_i^{Ig}(\theta) - Q_i^{Gg}(\theta)}, \tag{8a}$$
$$w_{ii}^{Ig}(\theta) = \frac{w_{ii}^{\gamma g}|_S(\theta) - Q_i^{Gg}(\theta) w_{ii}^{\gamma g}(\theta)}{Q_i^{Ig}(\theta) - Q_i^{Gg}(\theta)} \ . \tag{8b}$$

Here the Q values are calculated theoretically with a fiducial cosmology and the redshift distributions from data. Q_i^{Gg} is defined as

$$Q_i^{Gg}(\theta) \equiv w_{ii}^{Gg}|_S(\theta) / w_{ii}^{Gg}(\theta), \tag{9}$$

which is similar as the previous definition Eq. (4) using angular power spectra. With this definition, we no longer need to assume a constant $\bar{Q}_i$ value as before (Yao et al. 2020), instead, the angular scale dependency $Q_i^{Gg}(\theta)$ is taken into consideration, for a more precise lensing-IA separation.

Similarly, Q_i^{Ig} is defined as

$$Q_i^{Ig}(\theta) \equiv w_{ii}^{Ig}|_S(\theta) / w_{ii}^{Ig}(\theta) \tag{10}$$

to account for the non-symmetric redshift distribution, which could potentially make Q_i^{Ig} deviates from 1 ($w_{ii}^{Ig}|_S \neq w_{ii}^{Ig}$).

Here $\{ w^{\gamma g}, w^{\gamma g}|_S \}$ are direct observables and $\{ Q_i^{Gg}, Q_i^{Ig} \}$ can be robustly calculated given photo-z PDF, so we are able to separate and measure both w^{Gg} and w^{Ig} as in Eq. (8a) and (8b). A key step in our method is to calculate Q. The calculation is straightforward, but technical. We present detailed description in the appendix.

2.2. *Interpreting the separated Gg and Ig*

The next step is to extract the physics out of the Gg and Ig separated above. We need to compare with the theoretically predicted w^{Gg} and w^{Ig}. In this section, we briefly describe the basic theory of weak lensing and intrinsic alignment. The comparison between theory and observation will be presented in §4.

The lensing-galaxy cross power spectrum is calculated by the Limber equation,

$$C_{ii}^{Gg}(\ell) = \int_0^\infty \frac{W_i(\chi) n_i(\chi)}{\chi^2} b_g P_\delta \left(k = \frac{\ell}{\chi}; \chi \right) d\chi \ . \tag{11}$$

Here W_i is the lensing efficiency function. For a flat universe,

$$W_i(\chi_L) = \frac{3}{2} \Omega_m \frac{H_0^2}{c^2} (1+z_L) \int_{\chi_L}^\infty n_i(\chi_S) \frac{(\chi_S - \chi_L)\chi_L}{\chi_S} d\chi_S \ . \tag{12}$$

$n_i(\chi)$ is the galaxy distribution of the $i^{\rm th}$ photo-z bin in the comoving distance space, and is linked to the galaxy distribution in the true redshift space by $n_i(\chi) = n_i(z) dz/d\chi$. Here χ is the comoving distance, b_g is the galaxy bias, and P_δ is the matter power spectrum. Similarly, the IA-galaxy cross angular power spectrum C^{Ig} is given by

$$C_{ii}^{Ig}(\ell) = \int_0^\infty \frac{n_i(\chi) n_i(\chi)}{\chi^2} b_g P_{\delta,\gamma^I} \left(k = \frac{\ell}{\chi}; \chi \right) d\chi. \tag{13}$$

In this expression, P_{δ,γ^I} is the 3D matter-IA power spectrum, which depends on the IA model being used (or the "true" IA model). For comparison, we adopt the nonlinear tidal alignment model (Catelan et al. 2001; Hirata

Table 1. The ΛCDM cosmological parameters adopted in our analysis, which correspond to the best-fit cosmology from Planck2018 Planck Collaboration et al. (2020) (fiducial) and KV450 (Hildebrandt et al. 2020a) (alternative).

Survey	h_0	$\Omega_b h^2$	$\Omega_c h^2$	n_s	σ_8	w
Planck	0.6732	0.022383	0.12011	0.96605	0.812	-1.0
KV450	0.745	0.022	0.118	1.021	0.836	-1.0

& Seljak 2004) as the fiducial IA model. It is widely used in the other stage III surveys (Hildebrandt et al. 2017, 2020a; Troxel et al. 2018a; Hikage et al. 2019; Hamana et al. 2020; Chang et al. 2019). In this model,

$$P_{\delta,\gamma^I} = -A_{\rm IA}(L,z)\frac{C_1\rho_{m,0}}{D(z)}P_\delta(k;\chi), \qquad (14)$$

where $\rho_{m,0} = \rho_{crit}\Omega_{m,0}$ is the mean matter density of the universe at $z = 0$. $C_1 = 5\times10^{-14}(h^2 M_{\rm sun}/{\rm Mpc}^{-3})$ is the empirical amplitude found in Bridle & King (2007). In this work we adopt $C_1\rho_{crit} \approx 0.0134$ as in Krause et al. (2016); Yao et al. (2020). $D(z)$ is the linear growth factor normalized to 1 today. $A_{\rm IA}(L,z)$ is the IA amplitude parameter, which is expected to be luminosity(L)- and redshift(z)-dependent. In this work, we will investigate the possible redshift dependence and the galaxy-type dependence of this $A_{\rm IA}$ parameter.

The theoretical prediction of w^{Gg} and w^{Ig} are then given by the Hankel transformation,

$$w(\theta) = \frac{1}{2\pi}\int d\ell\ \ell C(\ell) J_2(\ell\theta)\ . \qquad (15)$$

Here $J_2(x)$ is the Bessel function of the first kind of order 2. We adopt the CCL library [2] (Chisari et al. 2019) for the theoretical calculations. These results are cross-checked with CAMB [3] (Lewis et al. 2000) in previous work (Yao et al. 2020). The cosmological parameters being used to calculate the theoretical predictions are the best-fit cosmology of Planck2018 and KV450, as shown in Table 1. The impact from uncertainties in the cosmological parameters on the theoretical predictions is negligible, compared with that from uncertainties in the galaxy bias b_g and the IA amplitude $A_{\rm IA}$. Also, σ_8 strongly degenerates with b_g in our case and they both enter the estimation of w^{Gg} and w^{Ig} in the same way. Therefore for the purpose of studying IA, it is valid to fix the cosmology.

3. SURVEY DATA

We apply our method to the Dark Energy Camera Legacy Survey (DECaLS) Data Release 3, which is part of the Dark Energy Spectroscopic Instrument (DESI) Legacy Imaging Surveys (Dey et al. 2019). The DECaLS DR3 contains images covering 4300 deg^2 in g-band, 4600 deg^2 in r-band and 8100 deg^2 in z-band. In total 4200 deg^2 have been observed in all three optical bands. The DECaLS data are processed by Tractor (Meisner et al. 2017; Lang et al. 2014).

The sources from the Tractor catalog are divided into five morphological types. Namely,

1. Point sources (PSF),
2. Simple galaxies (SIMP: an exponential profile with a fixed 0.45" effective radius and round profile),
3. de Vaucouleurs (DEV: elliptical galaxies),
4. Exponential (EXP: spiral galaxies),
5. Composite model (COMP: composite profiles which are de Vaucouleurs and exponential with the same source center).

In this catalog, the sky-subtracted images are stacked in five different ways: one stack per band, one "flat" Spectral Energy Distribution (SED) stack of each g-, r- and z-band, one "red" (g-r=1 mag and r-z=1 mag) SED stack of all bands. The sources are kept above the detection limit in any stack as candidates. The PSF model (delta function) and the SIMP model are adjusted on individual images, which are convolved by their own PSF model.

The galaxy ellipticities $e_{1,2}$ are free parameters of the above four SIMP, DEV, EXP and COMP models, except for the PSF model. The ellipticity are estimated by a joint fit on the three optical g-, r-, and z-band. We model potential measurement bias with a multiplicative (m) and additive bias (c) (Heymans et al. 2012; Miller et al. 2013; Hildebrandt et al. 2017),

$$\gamma^{\rm obs} = (1+m)\gamma^{\rm true} + c, \qquad (16)$$

The additive bias is expected to come from residuals in the anisotropic PSF correction. It depends on galaxy sizes. The addtive bias c is subtracted from each galaxy in the catalog. The multiplicative bias comes from the shear measurement. It can be generated by many effects, such as measurement method (Mandelbaum et al. 2015), blending and crowding (Euclid Collaboration et al. 2019). In order to calibrate our shear catalog, we cross-matched the DECaLS DR3 objects with the Canada-France-Hawaii Telescope (CFHT) Stripe 82 objects, and then computed the correction parameters (Phriksee et al. 2020). In addition, the data

[2] Core Cosmology Library, https://github.com/LSSTDESC/CCL

[3] Code for Anisotropies in the Microwave Background, https://camb.info/

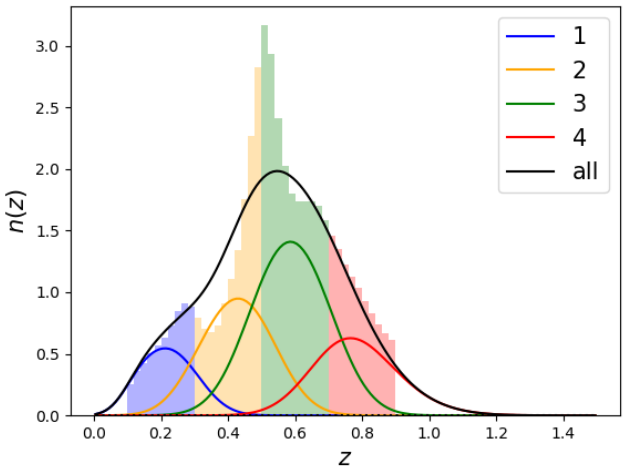


Figure 1. The redshift distribution of the galaxy samples analyzed. The shaded histogram is the photo-z distribution, which is divided into 4 tomographic bins. The color curves are the estimated true redshift distributions $n_i(z)$, while the black curve gives the total $n(z)$.

from DECaLS DR3 catalog were tested with the Obiwan simulations (Burleigh et al. in prep., Kong et al. (2020)), also described in Table A1 in Phriksee et al. (2020).

We employ the photo-z from Zou et al. (2019), which is based on the algorithm of k-nearest-neighbors and local linear regression. The photo-z is obtained from 5 photometric bands: three optical bands (g, r, and z), and two infrared bands (Wide-field Infrared Survey Explorer W1 and W2). We use samples with $r < 23$ mag. The training sample includes ~ 2.2 M spectroscopic galaxies.

For each galaxy we use in this work, we add two extra selections. One is to remove some galaxies with extreme shear multiplicative bias (requiring $1 + m > 0.5$). We note many selection effects could potentially bias the shear calibration, with more details in Li et al. (2020); Huff & Mandelbaum (2017); Sheldon & Huff (2017) and its potential impact in this work in Appendix C. The other is requiring small estimated photo-z error ($\Delta_z^P < 0.1$). Together with the selection of $0.1 < z^P < 0.9$, we obtain 23 million galaxies for the SC analysis. We divide them into 4 photo-z bins ($0.1 < z^P < 0.3$, $0.3 < z^P < 0.5$, $0.5 < z^P < 0.7$ and $0.7 < z^P < 0.9$). For each galaxy, our kNN photo-z algorithm also provides an Gaussian estimation of the photo-z error. We further apply this Gaussian scatter to obtain the redshift probability distribution function (PDF) for each galaxy. The overall photo-z distribution $n_i^P(z^P)$ and the true-z distribution $n_i(z)$ are shown in Fig. 1. More detailed discussion on the photo-z quality are included in Appendix A, where we show the Gaussian PDF is not accurate, however the overall scatter is accurate, which is of most importance in the self-calibration analysis Zhang (2010b). The possible impact of biased $n(z)$ is discussed in Appendix C.

4. RESULTS

We present the measurement of $w^{\gamma g}$ and $w^{\gamma g}|_S$ in §4.1, Q^{Gg} and Q^{Ig} in §4.2, w^{Gg} and w^{Ig} in §4.3. All the analysis in this work uses the default pipeline developed by JY in Yao et al. (2020). The 2-point correlation functions described in Eq. (17) is performed with TreeCorr[4] code (Jarvis et al. 2004).

4.1. $w^{\gamma g}$ and $w^{\gamma g}|_S$ measurement

We adopt the following estimator (Mandelbaum et al. 2006; Singh et al. 2017; Yao et al. 2020) to calculate $w^{\gamma g}$ and $w^{\gamma g}|_S$,

$$w^{\gamma g} = \frac{\sum_{\rm ED} w_j \gamma_j^+}{\sum_{\rm ED}(1+m_j)w_j} - \frac{\sum_{\rm ER} w_j \gamma_j^+}{\sum_{\rm ER}(1+m_j)w_j} \,. \quad (17)$$

Here $\sum_{\rm ED}$ means summing over all the tangential ellipticity (E) - galaxy number counts in the data (D) pairs, $\sum_{\rm ER}$ means summing over all the tangential ellipticity (E) - galaxy number counts in the random catalog (R) pairs. The numerators give the stacked tangential shear weighted by the weight w_j from the shear measurement algorithm of the $j^{\rm th}$ galaxy. The denominators give the normalization considering the number of pairs, the shear weight w_j, and the calibration for shear multiplicative bias $(1 + m_j)$. Here we note that, after normalization with the number of galaxies, the two denominators $\sum_{\rm ED}(1 + m_j)w_j$ and $\sum_{\rm ER}(1 + m_j)w_j$ are generally considered the same at large scale of our interest, as the boost factor (the ratio of these two) is normally considered as 1 (Mandelbaum et al. 2005; Singh et al. 2017).

For the random catalog, we use the DECaLS DR7 random catalog[5] and fit it into the DECaLS DR3 shear catalog footprint (Phriksee et al. 2020) with Healpy[6]. The size of our random catalog is ~ 10 times the size of the whole DECaLS DR3 shear catalog. This random catalog is used in Eq. (17) for the "R" part, while for the "D" part we use the galaxies in each tomographic bin. So the random sample size is much larger than real data. After the random-subtraction, the null-test with γ^X (the 45 deg rotation of γ^+) of Eq. (17) is consistent with zero.

[4] https://github.com/rmjarvis/TreeCorr
[5] http://legacysurvey.org/dr7/files/
[6] https://github.com/healpy/healpy

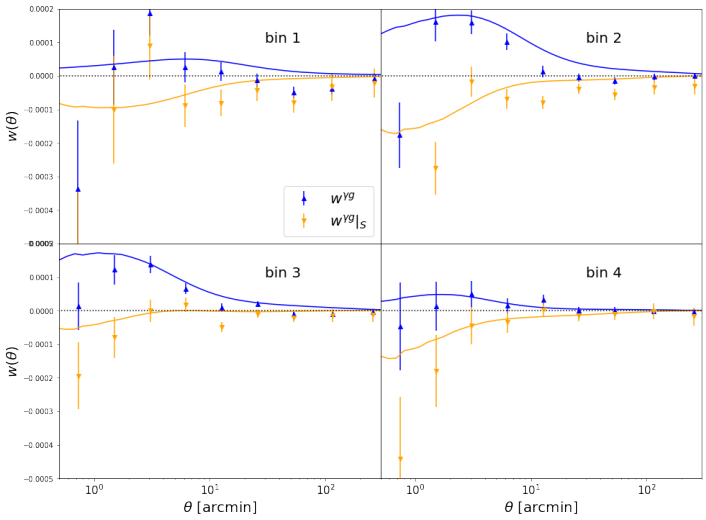


Figure 2. The directly measured $w^{\gamma g}$ (blue up-triangles) and $w^{\gamma g}|_S$ (orange down-triangles), along with the theory curves. The pair weighting adopted in $w^{\gamma g}|_S$ mainly down-weights the lensing contribution, while the IA contribution is almost unchanged. The difference between the two then quantifies the efficiency of the SC method. The difference is statistically significant in all 4 redshift bins (5.7σ, 16.1σ, 10.6σ, 6.0σ). We note that the theoretical curves are not the best-fit for $w^{\gamma g}$ and $w^{\gamma g}|_S$, but what predicted from the best-fit of separated signals $w^{\rm Gg}$ and w^{Ig} in Fig. 5 with the scale-dependent $Q_i^{Gg}(\theta)$ and $Q_i^{Ig}(\theta)$ in Fig. 3 and 4. The fitting χ^2 are [31.9, 65.0, 40.8, 8.4] with $d.o.f. = 16$ for each bin. There is a visual mismatch that is partially due to the strong correlation shown in Fig. 19.

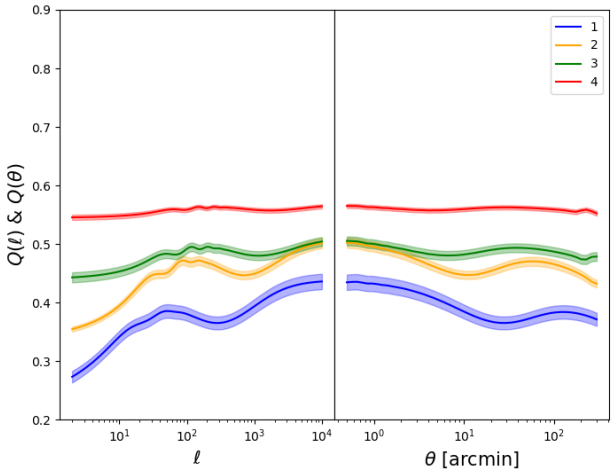


Figure 3. We show the measured $Q_i^{Gg}(\ell)$ from power spectra (as in Eq. (4)) in the left panel and $Q_i^{Gg}(\theta)$ from correlation functions (as in Eq. (9)) in the right panel. Different colors represent different bins. The shaded area shows 20 times the statistical error on the Q values. In the right panel we show the angular range $0.5 < \theta < 300$ [arcmin] that we are interested in, before any angular cut being adopted.

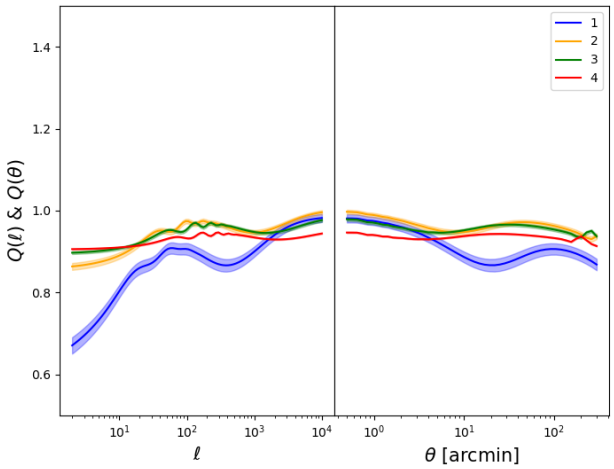


Figure 4. Similar to Fig. 3, but for $Q_i^{Ig}(\ell)$ and $Q_i^{Ig}(\theta)$ (as in Eq. (10)). The small deviation of Q^{Ig} from 1 ($\sim$ 10% level) comes from the non-symmetric distribution of $n^P(z^P)$ and $n(z)$, see Fig. 1 for example. Ignoring this will cause a $\sim$ 20% bias in w^{Ig} measurement. More discussions are included in the main text.

We note that we are not including the sky varying survey depth in the random sample, for three reasons. (1) Since our photo-z sample has a cut with $r < 23$ (Zou et al. 2019) to maintain high galaxy completeness, the "fake overdensity" due to this effect is expected to be low (Raichoor et al. 2017). (2) The small (due to the previous point) "fake overdensity" from varying observational depth is expected to not correlate with the galaxy shapes, as both the lensing part and the IA part are parts of the large scale structure. Therefore the fractional contribution in the correlations as selection bias is expected to be even less than in the density field. (3) Even if there still exists a selection bias in the 2-point statistics, it should be captured by our Jackknife re-sampling and is therefore appropriately included in the covariance matrix. In the next generation surveys, more detailed consideration for the random catalog should also be addressed.

We use Jackknife re-sampling to obtain the covariance matrices of $w^{\gamma g}$, $w^{\gamma g}|_S$, Q_i^{Gg}, Q_i^{Ig}, and the derived w^{Gg} and w^{Ig}. We use a K-means clustering code kmeans_radec[7] and generate 500 Jackknife regions. The choice of 500 Jackknife regions is to prevent biased estimation of the covariance for the length 34 data vector we

[7] https://github.com/esheldon/kmeans_radec

are going to use (discussed in §4.3), based on the analysis of Mandelbaum et al. (2006); Hartlap et al. (2007).

Fig. 2 shows the measured $w^{\gamma g}$ and $w^{\gamma g}|_S$. The observed $w^{\gamma g}$ and $w^{\gamma g}|_S$ at all four redshift bins are statistically different, with $5.7-16.1\sigma$ significance. It suggests that the photo-z quality sufficient for our need, and the selection $z_\gamma^P < z_g^P$ is efficient to reduce the lensing contribution, This clear separation is a necessary condition for our SC method.

The $w^{\gamma g}$-$w^{\gamma g}|_S$ separation is clearly more significant in this work than in Yao et al. (2020), which used KiDS450 and KV450 data. This we think is mainly due to the larger galaxy number in our DECaLS sample, especially in the second and the third redshift bins. Differences in the photo-z algorithm adopted and the resulting photo-z quality may also matter. However, since we lack robust information on photo-z outliers to quantify its impact on SC, we leave this issue for further study.

We also show the theoretical curves in Fig. 2 and calculated how good those fitting χ^2 are comparing to data. This demonstrates that the nonlinear tidal alignment model can provide a reasonably good description of the measurement.

Nevertheless, we caution that they are not the best-fit for $w^{\gamma g}$ and $w^{\gamma g}|_S$, but the prediction from the best-fit for w^{Gg} and w^{Ig}, which we will discuss in the next subsection. The two data sets ($\{w^{\gamma g}, w^{\gamma g}|_S\}$ v.s. $\{w^{Gg}, w^{Ig}\}$) are identical if we have perfect knowledge of Q^{Gg} and Q^{Ig}. In this work, we choose to fit against w^{Gg} and w^{Ig}, since their physical meanings (the lensing-galaxy correlation and the IA-galaxy correlation) are more straightforward, compared with $w^{\gamma g}$ and $w^{\gamma g}|_S$. The reasonably good agreement (Fig. 2) show that, our best-fit with scale cuts for $\{w^{Gg}, w^{Ig}\}$ also agrees very well with the $\{w^{\gamma g}, w^{\gamma g}|_S\}$ measurements. In the future analysis, we can alternatively use $w^{\gamma g}$ and $w^{\gamma g}|_S$ directly for the fitting. For such exercise, we also need the covariance matrix of the two sets of observables. We discuss them in in the Appendix D and Fig. 19 for your interests. As expected, the two have a strong positive correlation, since $w^{\gamma g}|_S$ is totally and positively included in $w^{\gamma g}$. Such a strong correlation must be taken into account in the related data analysis. Also due to this strong correlation, the fitted curves are visually different from data at some level, while the fitting χ^2 are reasonable as shown in Fig. 2.

4.2. *The lensing-drop Q_i^{Gg} and IA-drop Q_i^{Ig}*

Fig. 3 shows the measured lensing-drop $Q_i^{Gg}(\ell)$ from power spectra definition Eq. (4) and $Q_i^{Gg}(\theta)$ from correlation function definition Eq. (9). We leave calculation details in the appendix B. As we have explained in §2.1, Q^{Gg} is mainly determined by the photo-z quality, with $Q^{Gg} = 0$ for perfect photo-z and $Q^{Gg} = 1$ for totally wrong photo-z. For the SC method to be applicable, Q^{Gg} must be significantly smaller than unity (Zhang 2010a; Yao et al. 2020). Fig. 3 showed that $Q_i(\ell) \sim 0.5$ for a wide range of ℓ and photo-z bin. Therefore the photo-z quality is already sufficiently good to enable the SC method. Q varies between photo-z bins. We tested that for photo-z outlier rate $< 20\%$, the bias in Q for the current stage surveys is negligable. Besides the difference in photo-z quality, the effective width of the lensing kernel ($W_L(z_S, z_L)$) also plays a role.

According to Fig. 3, as well as in our previous work (Yao et al. 2020), the Q_i^{Gg} value is roughly constant in the range of $50 < \ell < 3000$. This is the main regime of interest in weak lensing cosmology. Previously we adopted the approximation $\bar{Q}_i = \langle Q_i(\ell)\rangle$, which could potentially under-estimate the IA signal at small-scale and over-estimate the IA signal at large-scale. In this work, by using scale-dependent $Q(\theta)$, as shown in the right panel of Fig. 3, we get rid of this effect. However, we note that as photo-z quality improves and/or redshift increases, the Q value will become more scale-independent so the above approximation should still hold. Thus this is not a major problem, but still worth bringing out.

In Fig. 3 we also include the statistical error. They are shown in the shaded regions, while the error-bars are exaggerated (20 times). The fact that the Q values have very low statistical error proves our previous statements in Yao et al. (2017, 2020).

Similarly, we show the Q_i^{Ig} measurements in Fig. 4. Generally $Q_i^{Ig} \sim 1$ is a good assumption. However, due to the non-symmetric photo-z distribution $n_i^P(z^P)$ and true-z distribution $n_i(z)$ shown in Fig. 1, the Q^{Ig} for real data will deviate from 1. We tested that for the $\sim 10\%$ over-estimation for Q^{Ig} (if assumed to be 1) shown in Fig. 4, the resulting w^{Ig} will be under-estimated by $\sim 20\%$. Interestingly, the final estimation of the IA amplitude $A_{\rm IA}$ is almost unbiased (see later in Fig. 8), which is due to the corresponding changes in the covariance matrix as well as the w^{Gg} signal.

Furthermore, we tested how the Q parameters depend on the assumed fiducial cosmology. We compared the calculation of Q^{Gg} and Q^{Ig} with Planck2018 cosmology and KV450 cosmology (where the main S_8 tension resides), as shown in Table 1. The differences are at $\sim 10^{-3}$ to $\sim 10^{-5}$ level, and the resulting bias in w^{Ig} is $\sim 10^{-3}$ level. This proved our previous statement in Yao et al. (2017, 2020) that, by construct, the Q^{Gg} and Q^{Ig} measurements are insensitive to the fiducial cosmol-

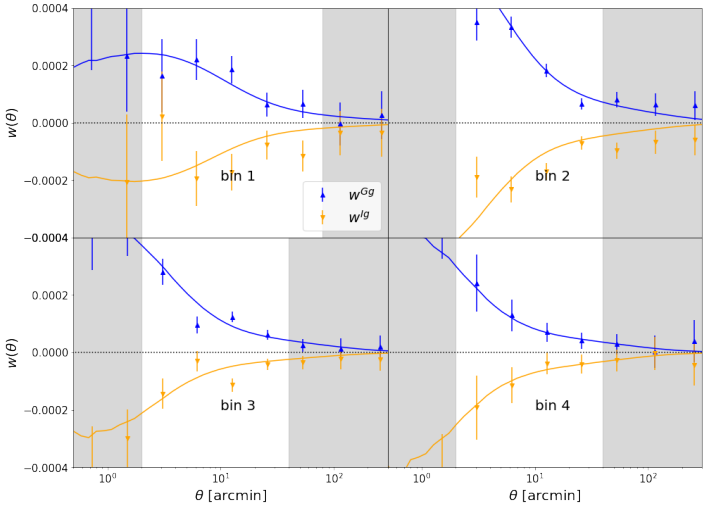


Figure 5. The lensing signal w^{Gg} (blue up-triangles) and the IA signal w^{Ig} (orange down-triangles) measured by the SC method. The grey shaded regions are the angular cuts where the effective $b_g(\theta)$ are not linear, see later in Fig. 11 for example. We also show the best-fit theoretical curves. In the fit, we fix cosmology, but varying the galaxy bias b_g and the IA amplitude $A_{\rm IA}$ for the non-linear tidal alignment model.

ogy. For the same reason, Q^{Ig} is also insensitive to the assumed IA model.

4.3. *Lensing-IA Separation (LIS)*

With the measured $\{\ w^{\gamma g},\ w^{\gamma g}|_S\ \}$ (Fig.2), Q_i^{Gg} (Fig. 3) and Q^{Ig} (Fig. 4), we are then able to separate w^{Gg} and w^{Ig} by Eq. (8a) & (8b). The results are shown in Fig. 5, along with the normalized covariane matrix (Fig. 6). We cut off small-scales to prevent further contamination from non-linear galaxy bias, massive neutrinos, baryonic effects, boost factor, etc. We cut off large-scale to prevent impact from insufficient random catalog. The cuts are shown in the grey shaded regions. The detection of intrinsic alignment (w^{Ig}) is significant at all four redshift bins and the corresponding S/N=3.5, 11.9, 5.5, 4.1 respectively.[8]

Now we compare with the theoretical prediction of the nonlinear tidal alignment model. Since the predicted $w^{Ig} \propto b_g A_{\rm IA} P_\delta$, we need to include the measurement $w^{Gg} \propto b_g P_\delta$, in order to break the b_g-$A_{\rm IA}$ degeneracy. Since both w^{Ig} and w^{Gg} are derived from the same set of data, they are expected to have a strong negative correlation. Fig. 6 confirms this expectation of strong anti-correlation. This figure shows the cross correlation coefficient (normalized covariance matrix), $r_{ab} \equiv Cov(a,b)/\sqrt{Cov(a,a)Cov(b,b)}$. Here $a,b \in (w^{Gg}(\theta_1), w^{Gg}(\theta_2), \cdots, w^{Ig}(\theta_1), \cdots)$. Therefore we should fit for w^{Gg} and w^{Ig} simultaneously and take this anti-correlation into account. We test that, if we ignore this strong anti-correlation and fit w^{Gg} and w^{Ig} separately, the bestfits do not well reproduce $w^{\gamma g}$ and $w^{\gamma g}|_S$ in Fig. 2. When doing the fitting, we only use the 34×34 matrix that correspond to the cuts in Fig. 5.

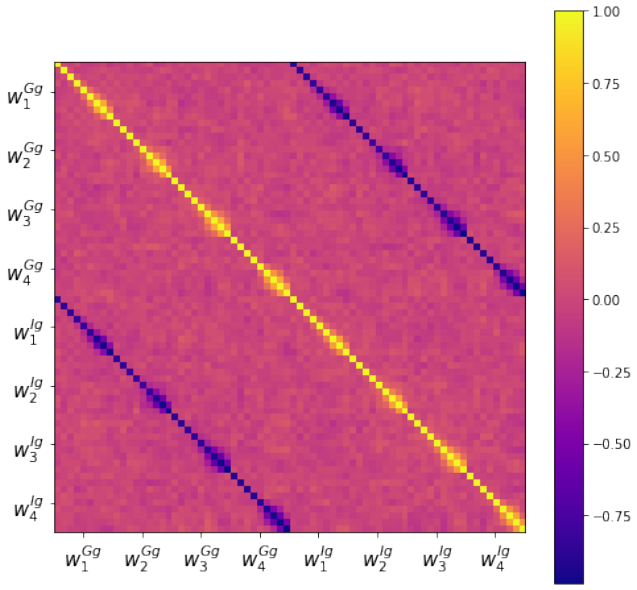


Figure 6. The normalized covariance matrix (The cross correlation coefficient) of the data vector $\mathbf{D} = (w^{Gg}(\theta), w^{Ig}(\theta))$. For each photo-z bin, there are 9 θ-bins for w^{Gg} and 9 for w^{Ig}, so the size for one z-bin is 18, and the overall size for the whole data vector is 72, leading to the 72×72 matrix above, corresponding to the combination of the 4 redshift bin shown in Fig. 5. The measured w^{Gg} and w^{Ig} show strong anti-correlation, which must be taken into account for quantifying the measurement significance and theoretical interpretation.

We also notice the main correlation is between w_i^{Gg} and w_i^{Ig} in the same bin i. There is no significant correlation between different redshift bins. This is another proof that the impact from photo-z outlier to our lensing-IA separation is not significant.

The theoretical fitting is carried out with a fixed cosmology (Planck cosmology in Table 1), and a fixed IA model (the nonlinear tidal alignment model). So there are only two free parameters in the fitting, namely the

[8] We caution that the detection significance is likely overestimated, since we do not include uncertainties in the Q value. The induced fluctuation is $\delta w^{Ig} = -w^{Gg}\delta Q/(1-Q) \simeq -w^{Gg} \times (2\delta Q)$. Since $w^{Ig} \sim w^{Gg}$ for the full sample, the induced fractional error is $\delta w^{Ig}/w^{Ig} \sim -2\delta Q$. The statistical Q fluctuation estimated by the Jackknife method is $\sim 10^{-3}$, and is therefore negligible in the w^{Ig} error budget. However, systematic error of Q arising from photo-z outliers may be larger. Unless $|\delta Q| \gtrsim 0.05$, the detection significance of w^{Ig} will not be significantly affected. After we have reliable estimation on photo-z outliers, we will quantify its impact.

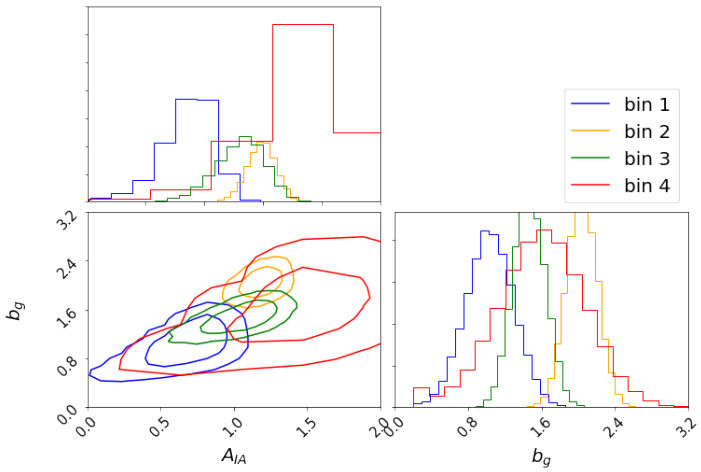


Figure 7. The MCMC fitting results (with 68% and 95% confidence contours) for the galaxy bias b_g and IA amplitude $A_{\rm IA}$ of each photo-z bin. We find a clear redshift-dependent evolution on the IA amplitude $A_{\rm IA}$. The strong constraining power in bin 2 and 3 are due to their large numbers of galaxies, as shown in Fig. 1. The abnormal behavior of bin 2 is due to the large fraction of red galaxies and possible bias from photo-z, which will be discussed later in this work.

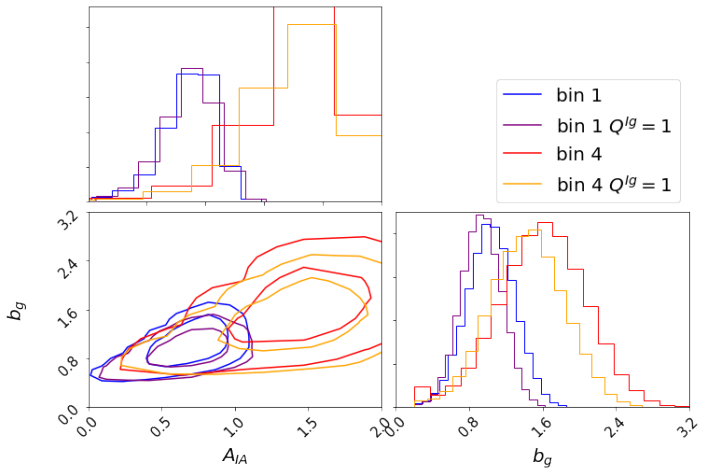


Figure 8. We show the comparison between using $Q^{Ig}(\theta)$ as in Eq. 10 and assuming $Q^{Ig}=1$ as in previous work (Yao et al. 2020). The systematic error of assuming $Q^{Ig}=1$ is not significant for the current stage weak lensing surveys, however it could potentially matter for the stage IV surveys.

galaxy bias b_g and the IA amplitude $A_{\rm IA}$. The two contain the leading order information of the measurements since $w^{Gg} \propto b_g$, and $w^{Ig} \propto b_g A_{\rm IA}$. Furthermore, a large fraction of cosmological dependence (in particular σ_8) can be absorbed into b_g since both $w^{Gg} \propto b_g P_\delta$ and $w^{Gg} \propto (b_g P_\delta) \times A_{\rm IA}$. Also for this reason, the constraint on $A_{\rm IA}$ is less cosmology-dependent than that on b_g. Since the major purpose of this work is to study IA, the above simplification in model fitting meets our needs. With future data of significantly improved S/N, we will perform a global fitting with relaxed constraints of cosmology and IA models.

The MCMC fitting results on b_g and $A_{\rm IA}$ are shown in Fig. 7, plotted with corner (Foreman-Mackey 2016). The best-fit values in this figure are used to plot the best-fit curves in Fig. 2 and 5. The best-fit curves agree with both the lensing signal and the IA signal reasonably well. This suggests that the LIS method works well, and support the non-linear tidal alignment IA model within the angular range of this work. In the future with better data and sufficient modeling of the small-scale, we can further investigate IA-physics in the non-linear regime.

Fig. 7 shows a clear redshift-dependent on the IA amplitude $A_{\rm IA}$. Comparing with a redshift-independent fitting with the best-fit $A_{\rm IA}=1.05$, our measurements rule out the constant IA amplitude assumption at $\sim 3\sigma$ (also see later in Fig. 15 with the $A_{\rm IA}(z)$ plot). When redshift increases, $A_{\rm IA}$ becomes larger. The only exception is the redshift bin 2. This is likely due to larger photo-z scatters and higher red galaxy fraction of the redshift bin 2. We will further discuss it in §4.4. We also investigated the impact of assuming $Q^{Ig}=1$ in Fig. 8. We only show for bin 1 and 4 for readability, but we note that $A^{\rm IA}$ from this assumption is consistent with the ones with varying $Q^{Ig}(\theta)$.

We caution that photo-z outlier can also lead to biased estimation in $A_{\rm IA}$. Even though this is beyond the scope of this paper, we try to quantify the quality of the photo-z being used in Appendix A. More sanity checks will be discussed in the next section.

The high S/N in Fig. 5 motivates us to further investigate such following questions:

1. How do the IA signals depend on the galaxy color (red/blue galaxies) or other galaxy properties?
2. How does the IA amplitude evolves with redshift, for red and blue galaxies?
3. How good is the current non-linear tidal alignment model?

4.4. *Separate IA measurements for red and blue galaxies*

The galaxy intrinsic alignment is expected to rely on galaxy type, and a major dependence is the galaxy color (red/blue galaxies). Therefore we apply the SC method separately for red and blue galaxies. The classification is done through the estimated clustering effect in the color-redshift space, obtained with the kNN algorithm (Zou et al. 2019). The classification criteria are shown in Fig. 9, with the total number of red/blue galaxies shown in Table 2. The overall red fraction is 32%.

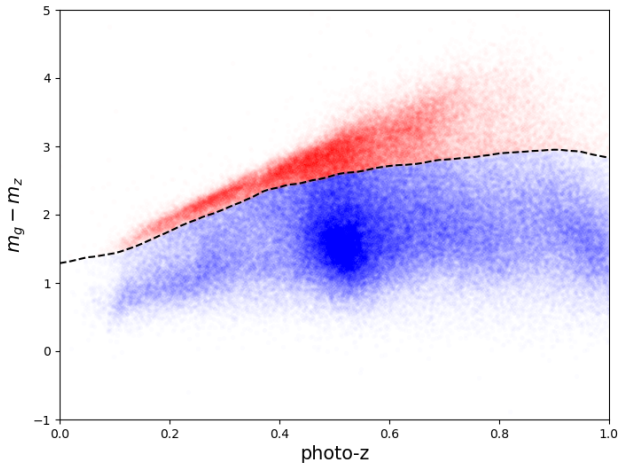


Figure 9. Red-blue galaxy classificatiopn through the color-redshift cut (black dashed curve) in the $m_g - m_z$ v.s. z^P space. Table 2 shows the total number of red/blue galaxies

Table 2. The number of red/blue galaxies, in the unit of millions (M).

	$0.1 < z^P < 0.9$	z1	z2	z3	z4
Red+Blue	23.4M	2.9M	6.1M	9.7M	4.7M
Red	7.4M	0.8M	2.3M	3.2M	1.1M
Blue	16.0M	2.0M	3.8M	6.5M	3.6M
Red fraction	32%	28%	38%	33%	23%

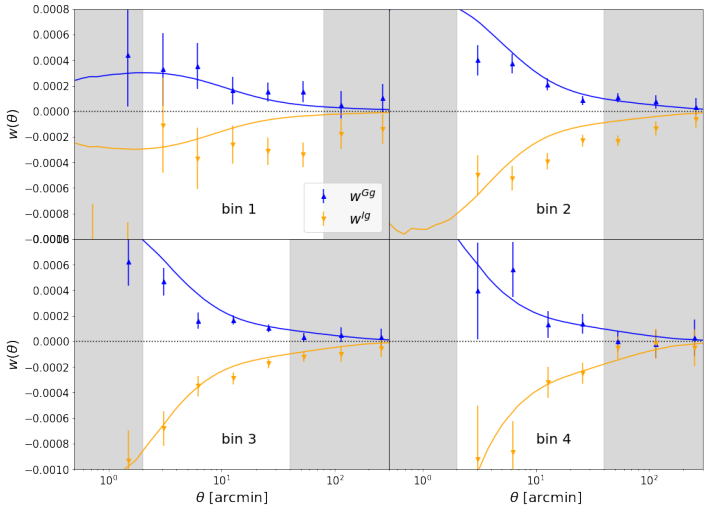


Figure 10. Similar to Fig. 5, but for red galaxies. The joint fit on the galaxy bias b_g and the IA amplitude $A_{\rm IA}$ are shown in Fig. 12, 15 & Table 3.

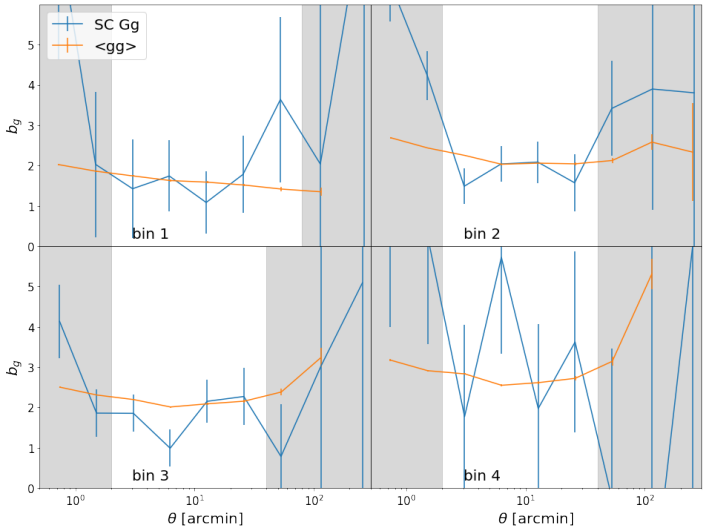


Figure 11. Comparison between effective galaxy bias b_g from SC lensing signal ($b_g = w^{Gg}_{\rm SC}/w^{Gg}_{\rm theory,b=1}$, blue) and galaxy clustering ($b_g = \sqrt{w^{gg}_{\rm data}/w^{gg}_{\rm theory,b=1}}$, orange) for the red galaxies. The consistency between these two shows the accuracy of the lensing-IA separation.

4.4.1. *Red galaxies*

Fig. 10 shows the separated lensing signal and IA signal for red galaxies, along with the best-fit theoretical curves. The detection of intrinsic alignment (w^{Ig}) for red galaxies is significant at all four redshift bins and the corresponding S/N=3.2, 9.9, 12.5, 6.7 respectively. Such S/N is comparable at low-z and significantly higher than the full sample at high-z, even with a much smaller sample (Table 2). This means that blue galaxies included in the full sample contributes little to the IA signal, but induce significant noise and dilute the IA measurement S/N. Generally, we achieved good fits for both the lensing part and the IA part. Overall the non-linear tidal alignment model is a good description to the IA of red galaxies.

We further present the effective galaxy bias obtained from the red galaxies for a sanity check in Fig. 11. Since we have better S/N with red galaxies, it will be more important to show the consistent results from different methods. We get the effective galaxy bias from the SC-separated lensing signal, by calculating the ratio between the measurements from data and the theoretical predictions assuming $b_g = 1$, namely $b_g = w^{Gg}_{\rm SC}/w^{Gg}_{\rm theory,b=1}$. Alternatively, it can be obtained from angular galaxy clustering of the same sample, following $b_g = \sqrt{w^{gg}_{\rm data}/w^{gg}_{\rm theory,b=1}}$. In Fig. 11 we showed these two methods give consistent results. This works as a further sanity-check in showing the results are robust against different systematics. For example:

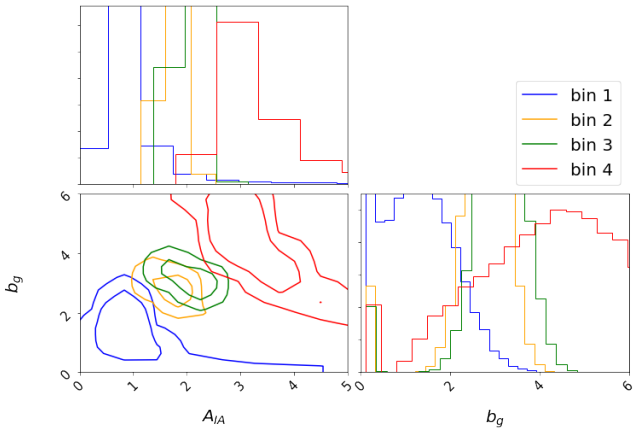


Figure 12. Similar to Fig. 7, but for red galaxies. We find a clear redshift-dependent evolution on the IA amplitude $A_{\rm IA}$. The overlap for the 2nd and 3rd redshift bins are likely due to significant overlap in their real redshift distribution.

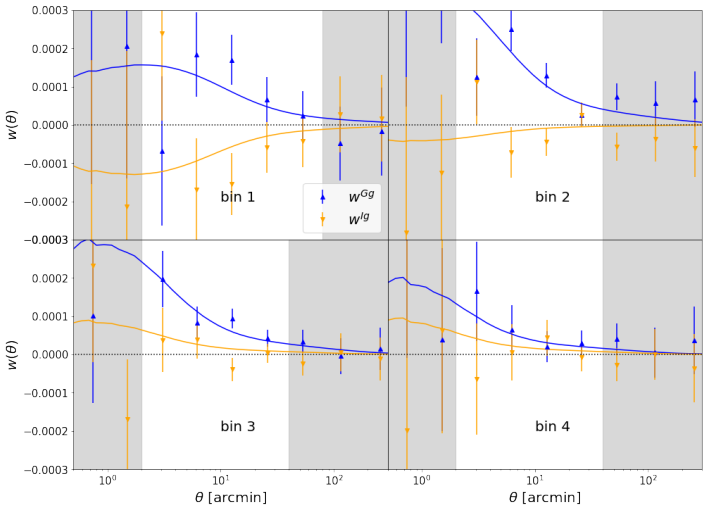


Figure 13. Similar to Fig. 5, but for blue galaxies.

(1) the sharp non-linear galaxy bias is cut off at small-scales.
(2) At large-scale when the effective b_g is obviously non-linear, it could be the impact of the insufficient random catalog. Thus it is cut off.
(3) Photo-z outlier should impact w^{Gg} and w^{gg} differently. While they are consistent, we know the impact from photo-z outlier is within reasonable range.

Fig. 12 shows the constraints of $b_g - A_{\rm IA}$ for the red galaxies. We see a clear redshift evolution of $A_{\rm IA}$, namely $A_{\rm IA}$ increases with increasing z. Even for the 2nd and 3rd bins where the confidence contours are quite close, their $A_{\rm IA}$ differs at $\sim 2\sigma$ level, thanks to the small uncertainties from a large number of galaxies. Comparing with a redshift-independent fitting with the best-fit $A_{\rm IA} = 1.87$, our measurements rule out the constant IA amplitude assumption at $\sim 3.9\sigma$ (also see later in Fig. 15 with the $A_{\rm IA}(z)$ plot). For future cosmic shear or shear cross-correlation studies, it is then important to take this redshift dependence into account. This is also important in studies in galaxy formation, and it could be potentially related to Kurita et al. (2020), where the halo IA (not the galaxy IA in our work) amplitude is also found to be z-dependent. The connection between halo IA and galaxy IA has also been discussed in Okumura et al. (2009). More details about our IA results can be seen later in 15 & Table 3

Furthermore, recalling for the full (red+blue) sample, the second redshift bin has an unusually large $A_{\rm IA}$ (Fig. 7). The fact that the 2nd bin and 3rd bin have similar $A_{\rm IA}$ for the red galaxies may also be responsible in this situation.

4.4.2. *Blue galaxies*

Fig. 13 presents the separated lensing signal and IA signal, along with their best-fit theoretical curves, for blue galaxies. The b_g and $A_{\rm IA}$ constraints are shown in Fig. 14, also later in Fig. 15 & Table 3. Different from the red galaxies, we do not detect the IA signal in bins 2, 3, and 4. This generally agrees with our current understanding that the IA signals mainly exist in the red galaxies. However, we do detect IA signal for blue galaxies in the lowest redshift bin, although the signal is weak. When fitted with the non-linear tidal alignment IA model, the detection significance is $\sim 1\sigma$. The current LIS method can not fully quantify the impact of photo-z outliers, plus blue galaxies normally have worse photo-z measurements comparing with red galaxies, therefore if this signal is real or not requires future exploration with better data.

We note the results in Fig. 15 could still be affected by shear calibration bias and photo-z bias, with potential changes in the results quantified in Appendix C. We expect in the future with a larger number of galaxies, better imaging and shear measurements, better photo-z, better modeling of other systematics (so that more information can be kept, instead of applying the scale-cuts), our SC method can further tell the physics for both red and blue galaxies.

5. SUMMARY AND CONCLUSIONS

In this work, we apply the lensing-IA separation (LIS) pipeline of the self-calibration (SC) method to the DECaLS DR3 shear + photo-z catalog. This allows us to measure the galaxy intrinsic alignment signal, free of assumption on the IA model. Therefore the measurement not only reduces IA contaminations in weak lensing cosmology, but also provides valuable information on the

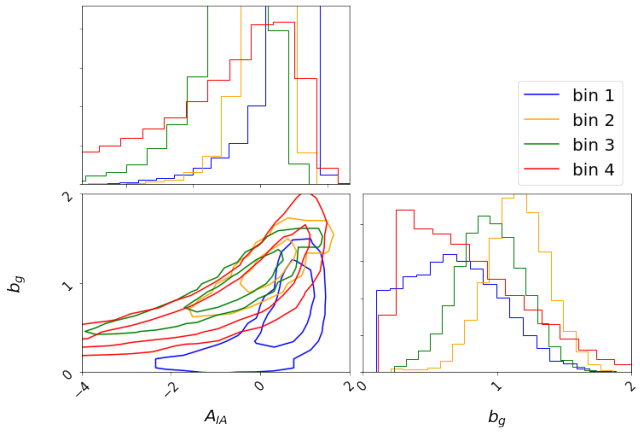


Figure 14. Similar to Fig. 7, but for blue galaxies. $A_{\rm IA}$ are consistent with 0.

physics of IA and galaxy formation. Comparing to our previous work with the KiDS data (Yao et al. 2020), we have improved the technique and analysis over the following aspects:

- We improved the SC formalism with a scale-dependent $Q^{Gg}(\theta)$ rather than a constant, as in Eq. (9) and Fig. 3. This prevents a biased estimation of w^{Gg} and w^{Ig} at low-z that shifts power between large-scale and small-scale.

- We improved the SC formalism by introducing the IA-drop $Q^{Ig} \neq 1$, due to non-symmetric redshift distribution, see Eq. (10) and Fig. 4. We showed in Fig. 8 that for the current stage the resulting $A_{\rm IA}$ is not biased even with the assumption $Q^{Ig} = 1$. But it could matter for future surveys.

- We tested for different cosmology, as in Table 1, the Q parameter will be biased by $\sim 10^{-5}$ to $\sim 10^{-3}$, and the resulting w^{Ig} will be biased by $\sim 10^{-3}$ level. This demonstrated the bias from the fiducial cosmology that SC method need to assume is negligible. For the same reason, Q^{Ig}, by construct, is also insensitive to the assumed IA model. The bias from assumed IA model should be much smaller compared to Fig. 8.

- We use jackknife resampling in each step of the calculation so that all the statistical uncertainties are included. We showed the statistical error on Q is $\sim 10^{-3}$ in Fig. 3 and 4. This demonstrated our previous statement in Yao et al. (2017) that Q won't introduce much statistical error. Addressing the systematic error from photo-z outlier, on the other hand, is beyond the scope of this paper as perfect knowledge on redshift is required.

Table 3. The best-fit $A_{\rm IA}$ and the 1σ error.

$A_{\rm IA}$	z1	z2	z3	z4
Red+Blue	$0.70^{+0.15}_{-0.20}$	$1.19^{+0.10}_{-0.10}$	$1.05^{+0.15}_{-0.19}$	$1.47^{+0.25}_{-0.36}$
Red	$0.82^{+0.41}_{-0.26}$	$1.69^{+0.19}_{-0.17}$	$2.00^{+0.19}_{-0.16}$	$3.06^{+1.00}_{-0.46}$
Blue	$0.69^{+0.28}_{-0.59}$	$0.18^{+0.37}_{-0.52}$	$-0.49^{+0.64}_{-1.03}$	$-0.75^{+1.32}_{-3.08}$

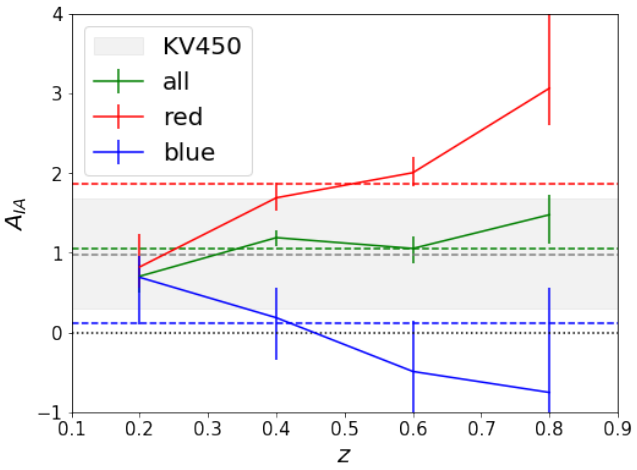


Figure 15. The color- and redshift-dependence of the best-fit $A_{\rm IA}$. Dashed lines are the best-fit with the constant $A_{\rm IA}$ assumption.

- We introduce the covariance between w^{Gg} and w^{Ig} in Fig. 6, where the strong anti-correlation was not taken into consideration in previous work. This leads to more reliable fitting.

- We include the impact of galaxy bias b_g in this work. It has been discussed to be one of the most important systematics in the SC method in Yao et al. (2017). We performed a simultaneous fitting for the linear galaxy bias b_g and IA amplitude $A_{\rm IA}$ to account for its effect, see in Fig. 7, 12 and 14.

- We apply additional scale cuts to prevent bias from different systematics, including non-linear galaxy bias, insufficient modeling of the matter power spectrum at small-scale, fake signal due to insufficient random catalog at large-scale, etc.

- We include multiple sanity checks in this work to validate our results, including checking the cross-shear (45-degree rotation) measurements are consistent with 0, comparing the resulting effective galaxy bias between the separated w^{Gg} and galaxy clustering w^{gg}, no significant correlation between different z-bins in the covariance matrix, comparing $A_{\rm IA}$ with other analysis, etc.

With the above improvements, we obtain reliable measurements on the separated lensing signal w^{Gg} and IA signal w^{Ig}. Our findings can be summarized in Table 3 and 4 and visualized in Fig. 15, with the following aspects:

- The separation and measurement of lensing and IA are more robust and statistically significant. A crucial diagnostic is the differences in the two direct observables $w^{\gamma g}$ and $w^{\gamma g}|_S$. The measured difference is improved to $\sim 16\sigma$ for a single redshift bin (bin 2) and $\sim 21\sigma$ (comparing with $\sim 16\sigma$ in our previous work Yao et al. (2020)) for the full galaxy sample. For this reason, the total detection significance of the IA signal reaches $\sim 14\sigma$. The overall IA amplitude of our DECaLS DR3 sample is consistent with the KV450 (Hildebrandt et al. 2020a) results, but with stronger constraint, see in Fig. 15. It is also consistent with the common understanding that $A_{\rm IA} \sim 1$.

- We detect the IA dependence on galaxy color. For red galaxies, we detect IA in all photo-z bins at $0.1 < z^P < 0.9$. The detected IA signal shows reasonable agreement with the nonlinear tidal alignment model. The red-blue separation increases the S/N of IA detection in red galaxies to $\sim 17.6\sigma$.

- We find for blue galaxies, the IA signal is generally consistent with 0, except for the weak and tentative ($\sim 1\sigma$) detection in the lowest redshift bin at $z^P < 0.3$.

- Our results rule out the assumption of constant IA amplitude at $\sim 3.9\sigma$ for the red sample, and at $\sim 3\sigma$ for the full sample. Especially for red galaxies, the IA amplitude $A_{\rm IA}$ increases with redshift. From Fig. 15 we can also see a (not clear) evolution pattern for the blue galaxies, nonetheless, the full sample also seems to have a $A_{\rm IA}(z)$ evolution pattern, which agrees with our previous finding for KV450 (Yao et al. 2020) that IA is stronger at high-z. Tests on how the calibrations of multiplicative bias and redshift distribution can affect the $A_{\rm IA}(z)$ relation are shown in Appendix C. More test on the z-dependencies for the full sample and the blue sample can be done with a larger galaxy number and better photo-z in the future. We note similar z-evolution results has been found in a recent study with hydrodynamic simulations (Samuroff et al. 2020).

- Our separated IA signals do not rely on strong assumptions about IA physics. The MCMC fitting for b_g and $A_{\rm IA}$ assumed the non-linear tidal alignment model, also known as the non-linear linear alignment (NLA) model, see in Eq. (14). But it can also be used to investigate other alternatives, for example Blazek et al. (2019); Fortuna et al. (2020). Here we present the fitting χ^2 in Table 4. We notice that for the red galaxies, in bin 2 and bin 3 where the IA detection is most significant, the $\chi^2/d.o.f.$ is not ideal. This suggests possible systematics and/or potential deviation from the assumed NLA model. However, the relatively large χ^2 could also come from photo-z outlier (see Appendix A) that we are unable to fully address in this work. We leave this point for future studies.

Table 4. Goodness of fit (χ^2) to the measured w^{Gg} and w^{Ig} by the nonlinear tidal alignment model. The large χ^2 mainly arises from $\lesssim 5$ Mpc scale (Fig. 5, 10 and 13). They suggest improvement in the theoretical modelling by taking complexities such as baryonic physics, non-linear galaxy bias and beyond tidal alignment IA models into account.

$\chi^2/d.o.f.$	z1	z2	z3	z4
Red+Blue	22.4/8	32.2/6	20.2/6	3.6/6
Red	27.5/8	72.0/6	68.0/6	3.6/6
Blue	7.4/8	7.0/6	4.6/6	3.5/6

With better data such as DECaLS DR8, future data release from KiDS/HSC/DES/LSST/etc, and possible improved photo-z estimation and shear measurements (which are beyond the scope of this paper, see discussions in Appendix C), we plan to robustly measure the IA amplitude, and its dependence on the physical scale, redshift and galaxy properties such as color and flux. We may also be able to reveal more detailed information, such as the observed negative b_g-$A_{\rm IA}$ correlation in red galaxies, and the possibly positive correlation in blue galaxies (Fig. 12 & 14). This information will be useful to understand galaxy formation. Furthermore, the same analysis also provides the measurement of w^{Gg}, namely the lensing-galaxy cross-correlation free of IA contaminations. This data contains useful information to constrain cosmology, as discussed in the previous work (Yao et al. 2020). This method could also potentially be affected by modified gravity, as the separated lensing signal relies on the gravitational potential $\nabla^2(\phi-\psi)$, while the IA signal relies on $\nabla^2\phi$ (Zhang et al. 2007). We will present more cosmological studies in separate future works.

6. ACKNOWLEDGEMENTS

The authors thank the referee for many useful comments, which highly improved the quality of this paper. The authors thank Hu Zou, Haojie Xu, Jiaxin

Wang, Minji Oh, Zhaozhou Li for useful discussions. JY and PZ acknowledge the support of the National Science Foundation of China (11621303, 11433001). HYS acknowledges the support from NSFC of China under grant 11973070, the Shanghai Committee of Science and Technology grant No.19ZR1466600 and Key Research Program of Frontier Sciences, CAS, Grant No. ZDBS-LY-7013. The computations in this paper were run on the π 2.0 cluster supported by the Center for High Performance Computing at Shanghai Jiao Tong University.

The codes JY produced for this paper were written in Python. JY thanks all its developers and especially the people behind the following packages: SCIPY (Jones et al. 2001–), NUMPY (van der Walt et al. 2011), ASTROPY (Astropy Collaboration et al. 2013) and MATPLOTLIB (Hunter 2007).

REFERENCES

Asgari, M., Heymans, C., Hildebrandt, H., et al. 2019, A&A, 624, A134, doi: 10.1051/0004-6361/201834379

Asgari, M., Lin, C.-A., Joachimi, B., et al. 2020, arXiv e-prints, arXiv:2007.15633. https://arxiv.org/abs/2007.15633

Astropy Collaboration, Robitaille, T. P., Tollerud, E. J., et al. 2013, A&A, 558, A33, doi: 10.1051/0004-6361/201322068

Bernal, J. L., Verde, L., & Riess, A. G. 2016, JCAP, 2016, 019, doi: 10.1088/1475-7516/2016/10/019

Bielby, R. M., Finoguenov, A., Tanaka, M., et al. 2010, A&A, 523, A66, doi: 10.1051/0004-6361/201015135

Blazek, J., Vlah, Z., & Seljak, U. 2015, JCAP, 8, 015, doi: 10.1088/1475-7516/2015/08/015

Blazek, J. A., MacCrann, N., Troxel, M. A., & Fang, X. 2019, PhRvD, 100, 103506, doi: 10.1103/PhysRevD.100.103506

Bridle, S., & King, L. 2007, New Journal of Physics, 9, 444, doi: 10.1088/1367-2630/9/12/444

Cardamone, C. N., van Dokkum, P. G., Urry, C. M., et al. 2010, ApJS, 189, 270, doi: 10.1088/0067-0049/189/2/270

Catelan, P., Kamionkowski, M., & Blandford, R. D. 2001, MNRAS, 320, L7, doi: 10.1046/j.1365-8711.2001.04105.x

Chang, C., Wang, M., Dodelson, S., et al. 2019, MNRAS, 482, 3696, doi: 10.1093/mnras/sty2902

Chisari, N. E., Koukoufilippas, N., Jindal, A., et al. 2017, MNRAS, 472, 1163, doi: 10.1093/mnras/stx1998

Chisari, N. E., Alonso, D., Krause, E., et al. 2019, ApJS, 242, 2, doi: 10.3847/1538-4365/ab1658

Crittenden, R. G., Natarajan, P., Pen, U.-L., & Theuns, T. 2001, ApJ, 559, 552, doi: 10.1086/322370

Croft, R. A. C., & Metzler, C. A. 2000, ApJ, 545, 561, doi: 10.1086/317856

Dey, A., Schlegel, D. J., Lang, D., et al. 2019, AJ, 157, 168, doi: 10.3847/1538-3881/ab089d

Dossett, J. N., & Ishak, M. 2013, PhRvD, 88, 103008, doi: 10.1103/PhysRevD.88.103008

Euclid Collaboration, Martinet, N., Schrabback, T., et al. 2019, A&A, 627, A59, doi: 10.1051/0004-6361/201935187

Foreman-Mackey, D. 2016, The Journal of Open Source Software, 1, 24, doi: 10.21105/joss.00024

Fortuna, M. C., Hoekstra, H., Joachimi, B., et al. 2020, arXiv e-prints, arXiv:2003.02700. https://arxiv.org/abs/2003.02700

Freedman, W. L., Madore, B. F., Hatt, D., et al. 2019, ApJ, 882, 34, doi: 10.3847/1538-4357/ab2f73

Hamana, T., Shirasaki, M., Miyazaki, S., et al. 2020, PASJ, 72, 16, doi: 10.1093/pasj/psz138

Hartlap, J., Simon, P., & Schneider, P. 2007, A&A, 464, 399, doi: 10.1051/0004-6361:20066170

Hartley, W. G., Chang, C., Samani, S., et al. 2020, Monthly Notices of the Royal Astronomical Society, 496, 4769, doi: 10.1093/mnras/staa1812

Heavens, A. F. 2002, in The Shapes of Galaxies and their Dark Halos, ed. P. Natarajan, 21–28, doi: 10.1142/9789812778017_0004

Heymans, C., Brown, M., Heavens, A., et al. 2004, MNRAS, 347, 895, doi: 10.1111/j.1365-2966.2004.07264.x

Heymans, C., Van Waerbeke, L., Miller, L., et al. 2012, MNRAS, 427, 146, doi: 10.1111/j.1365-2966.2012.21952.x

Hikage, C., Oguri, M., Hamana, T., et al. 2019, PASJ, 71, 43, doi: 10.1093/pasj/psz010

Hildebrandt, H., Viola, M., Heymans, C., et al. 2017, MNRAS, 465, 1454, doi: 10.1093/mnras/stw2805

Hildebrandt, H., Köhlinger, F., van den Busch, J. L., et al. 2020a, A&A, 633, A69, doi: 10.1051/0004-6361/201834878

Hildebrandt, H., van den Busch, J. L., Wright, A. H., et al. 2020b, arXiv e-prints, arXiv:2007.15635. https://arxiv.org/abs/2007.15635

Hirata, C. M., & Seljak, U. 2004, PhRvD, 70, 063526, doi: 10.1103/PhysRevD.70.063526

Hoekstra, H., & Jain, B. 2008, Annual Review of Nuclear and Particle Science, 58, 99, doi: 10.1146/annurev.nucl.58.110707.171151

Huff, E., & Mandelbaum, R. 2017, arXiv e-prints, arXiv:1702.02600. https://arxiv.org/abs/1702.02600

Hunter, J. D. 2007, Computing in Science Engineering, 9, 90, doi: 10.1109/MCSE.2007.55

Jarvis, M., Bernstein, G., & Jain, B. 2004, MNRAS, 352, 338, doi: 10.1111/j.1365-2966.2004.07926.x

Jing, Y. P. 2002, MNRAS, 335, L89, doi: 10.1046/j.1365-8711.2002.05899.x

Joachimi, B., Semboloni, E., Hilbert, S., et al. 2013, MNRAS, 436, 819, doi: 10.1093/mnras/stt1618

Joachimi, B., Cacciato, M., Kitching, T. D., et al. 2015, SSRv, 193, 1, doi: 10.1007/s11214-015-0177-4

Jones, E., Oliphant, T., Peterson, P., et al. 2001–, SciPy: Open source scientific tools for Python. http://www.scipy.org/

Joudaki, S., Hildebrandt, H., Traykova, D., et al. 2020, A&A, 638, L1, doi: 10.1051/0004-6361/201936154

Kiessling, A., Cacciato, M., Joachimi, B., et al. 2015, SSRv, 193, 67, doi: 10.1007/s11214-015-0203-6

Kilbinger, M. 2015, Reports on Progress in Physics, 78, 086901, doi: 10.1088/0034-4885/78/8/086901

Kirk, D., Brown, M. L., Hoekstra, H., et al. 2015, SSRv, 193, 139, doi: 10.1007/s11214-015-0213-4

Kong, H., Burleigh, K. J., Ross, A., et al. 2020, MNRAS, doi: 10.1093/mnras/staa2742

Krause, E., Eifler, T., & Blazek, J. 2016, MNRAS, 456, 207, doi: 10.1093/mnras/stv2615

Kurita, T., Takada, M., Nishimichi, T., et al. 2020, arXiv e-prints, arXiv:2004.12579. https://arxiv.org/abs/2004.12579

Laigle, C., McCracken, H. J., Ilbert, O., et al. 2016, ApJS, 224, 24, doi: 10.3847/0067-0049/224/2/24

Lang, D., Hogg, D. W., & Schlegel, D. J. 2014, arXiv e-prints, arXiv:1410.7397. https://arxiv.org/abs/1410.7397

Lee, J., & Pen, U.-L. 2001, arXiv e-prints, astro. https://arxiv.org/abs/astro-ph/0111186

Lewis, A., Challinor, A., & Lasenby, A. 2000, ApJ, 538, 473, doi: 10.1086/309179

Li, H., Zhang, J., Liu, D., et al. 2020, arXiv e-prints, arXiv:2006.02095. https://arxiv.org/abs/2006.02095

Lin, W., Mack, K. J., & Hou, L. 2019, arXiv e-prints, arXiv:1910.02978. https://arxiv.org/abs/1910.02978

LSST Science Collaboration, Abell, P. A., Allison, J., et al. 2009, arXiv e-prints, arXiv:0912.0201. https://arxiv.org/abs/0912.0201

Mandelbaum, R. 2018, ARA&A, 56, 393, doi: 10.1146/annurev-astro-081817-051928

Mandelbaum, R., Hirata, C. M., Ishak, M., Seljak, U., & Brinkmann, J. 2006, MNRAS, 367, 611, doi: 10.1111/j.1365-2966.2005.09946.x

Mandelbaum, R., Hirata, C. M., Seljak, U., et al. 2005, Monthly Notices of the Royal Astronomical Society, 361, 1287, doi: 10.1111/j.1365-2966.2005.09282.x

Mandelbaum, R., Rowe, B., Armstrong, R., et al. 2015, MNRAS, 450, 2963, doi: 10.1093/mnras/stv781

Mehta, V., Scarlata, C., Capak, P., et al. 2018, ApJS, 235, 36, doi: 10.3847/1538-4365/aab60c

Meisner, A. M., Lang, D., & Schlegel, D. J. 2017, AJ, 154, 161, doi: 10.3847/1538-3881/aa894e

Meng, X.-g., Yu, Y., Zhang, P., & Jing, Y. 2018, ApJ, 864, 1, doi: 10.3847/1538-4357/aad504

Miller, L., Heymans, C., Kitching, T. D., et al. 2013, MNRAS, 429, 2858, doi: 10.1093/mnras/sts454

Okumura, T., Jing, Y. P., & Li, C. 2009, ApJ, 694, 214, doi: 10.1088/0004-637X/694/1/214

Phriksee, A., Jullo, E., Limousin, M., et al. 2020, MNRAS, 491, 1643, doi: 10.1093/mnras/stz3049

Planck Collaboration, Aghanim, N., Akrami, Y., et al. 2020, A&A, 641, A1, doi: 10.1051/0004-6361/201833880

Pujol, A., Bobin, J., Sureau, F., Guinot, A., & Kilbinger, M. 2020, arXiv e-prints, arXiv:2006.07011. https://arxiv.org/abs/2006.07011

Raichoor, A., Comparat, J., Delubac, T., et al. 2017, MNRAS, 471, 3955, doi: 10.1093/mnras/stx1790

Refregier, A. 2003, ARA&A, 41, 645, doi: 10.1146/annurev.astro.41.111302.102207

Riess, A. G., Casertano, S., Yuan, W., Macri, L. M., & Scolnic, D. 2019, ApJ, 876, 85, doi: 10.3847/1538-4357/ab1422

Rong, Y., Yi, S.-X., Zhang, S.-N., & Tu, H. 2015, MNRAS, 451, 2536, doi: 10.1093/mnras/stv865

Samuroff, S., Mandelbaum, R., & Blazek, J. 2020, arXiv e-prints, arXiv:2009.10735. https://arxiv.org/abs/2009.10735

Samuroff, S., Blazek, J., Troxel, M. A., et al. 2019, MNRAS, 489, 5453, doi: 10.1093/mnras/stz2197

Sheldon, E. S., & Huff, E. M. 2017, ApJ, 841, 24, doi: 10.3847/1538-4357/aa704b

Singh, S., Mandelbaum, R., Seljak, U., Slosar, A., & Vazquez Gonzalez, J. 2017, Monthly Notices of the Royal Astronomical Society, 471, 3827, doi: 10.1093/mnras/stx1828

Troxel, M. A., & Ishak, M. 2015, PhR, 558, 1, doi: 10.1016/j.physrep.2014.11.001

Troxel, M. A., MacCrann, N., Zuntz, J., et al. 2018a, PhRvD, 98, 043528, doi: 10.1103/PhysRevD.98.043528

Troxel, M. A., Krause, E., Chang, C., et al. 2018b, MNRAS, 479, 4998, doi: 10.1093/mnras/sty1889

van der Walt, S., Colbert, S. C., & Varoquaux, G. 2011, Computing in Science and Engineering, 13, 22, doi: 10.1109/MCSE.2011.37

Weinberg, D. H., Mortonson, M. J., Eisenstein, D. J., et al. 2013, PhR, 530, 87, doi: 10.1016/j.physrep.2013.05.001

Xia, Q., Kang, X., Wang, P., et al. 2017, ApJ, 848, 22, doi: 10.3847/1538-4357/aa8d17

Yao, J., Ishak, M., Lin, W., & Troxel, M. 2017, JCAP, 2017, 056, doi: 10.1088/1475-7516/2017/10/056

Yao, J., Ishak, M., Troxel, M. A., & LSST Dark Energy Science Collaboration. 2019, MNRAS, 483, 276, doi: 10.1093/mnras/sty3188

Yao, J., Pedersen, E. M., Ishak, M., et al. 2020, MNRAS, 495, 3900, doi: 10.1093/mnras/staa1354

Zhang, P. 2010a, ApJ, 720, 1090, doi: 10.1088/0004-637X/720/2/1090

—. 2010b, MNRAS, 406, L95, doi: 10.1111/j.1745-3933.2010.00893.x

Zhang, P., Liguori, M., Bean, R., & Dodelson, S. 2007, PhRvL, 99, 141302, doi: 10.1103/PhysRevLett.99.141302

Zou, H., Gao, J., Zhou, X., & Kong, X. 2019, The Astrophysical Journal Supplement Series, 242, 8, doi: 10.3847/1538-4365/ab1847

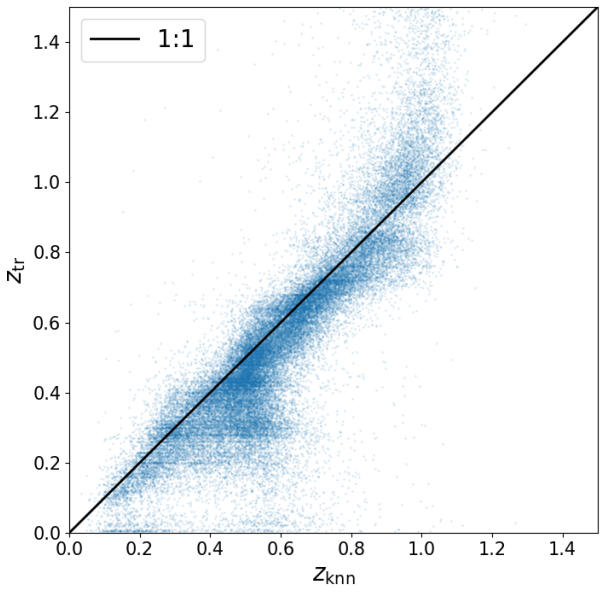


Figure 16. In this figure we present the comparison between the kNN photo-z ($z_{\rm knn}$ shown on the x-axis) samples being used in this work, and the selected good redshift ($z_{\rm tr}$ shown on the y-axis) samples. There are clearly two outlier regions, at $z_{\rm knn} \sim 0.5$ (corresponding to mainly bin 2 and 3 of this work) and $z_{\rm knn} \sim 1$ (which is cut off in this work). We calculated the photo-z outlier rate $f_{\Delta z>0.15}$, defined as the fraction with $|z_{\rm knn} - z_{\rm tr}| > 0.15$, which are [0.09, 0.19, 0.26, 0.15] for the 4 z-bins being used. The corresponding systematic shift $< z_{\rm knn} - z_{\rm tr} >$ are [0.02, 0.06, 0.08, 0.01].

APPENDIX

A. VALIDATING THE PHOTO-Z QUALITY

We emphasize that the photo-z techniques are beyond the scope of this paper. Nonetheless, here we present the validation of the photo-z samples being used in this work, in addition to the correlation functions. We combine galaxies from UDS HSC + SPLASH (Mehta et al. 2018), ECDFS (Cardamone et al. 2010), CFHTLS Deep + WIRDS (Bielby et al. 2010), and COSMOS (Laigle et al. 2016), to get a large reliable photo-z catalog. The overall redshift distribution is quite similar to the $n(z)$ determined from COSMOS only, and was already presented in Phriksee et al. (2020). By matching the above "good photo-z catalog" with our catalog of DR3 shear and kNN photo-z, we have a resulting sample with 46961 galaxies.

We refer to the "good photo-z catalog" as "true-z" in the following tests. In Fig. 16 we present the direct comparison between the kNN photo-z $z_{\rm knn}$ (Zou et al. 2019) in this work and the "true-z" $z_{\rm tr}$ described above. There are two regions that deviate from the 1:1 line significantly. The one we don't need to care about is the outlier region with $z_{\rm knn} \sim 1$, since it has been cut off with our binning selection $0.1 < z_{\rm knn} < 0.9$. The outlier region we need to care about is $z_{\rm knn} \sim 0.5$. The main photo-z outlier will be affecting bin 2 and 3, causing some disorder in the estimated photo-z and biasing the resulting w^{Gg} and w^{Ig} measurements. We think the high outlier rates and systematic shifts in bins 2 and 3 correspond to the high χ^2 values shown in Table 4. On the other hand, the relatively reliable photo-z in bin 1 and 4 justified our result of IA redshift evolution.

We further present the redshift distribution of this work and the reference "good photo-z sample" in Fig. 17. The $n(z)$ used in this work is shown as the "knn" distribution, which has very similar amplitude and scatter comparing with the reference "true" $n(z)$. This demonstrates that the given Gaussian redshift scatter from Zou et al. (2019) is generally reasonable. On the other hand, we do observe a significant difference at $z \sim 0.4$, resulting from the significant outlier problem shown previously in Fig. 16. This also agrees with the arguments in Zou et al. (2019) that the main redshift-color degeneracy will happen in this redshift range, leading to some misclassification of the photo-z.

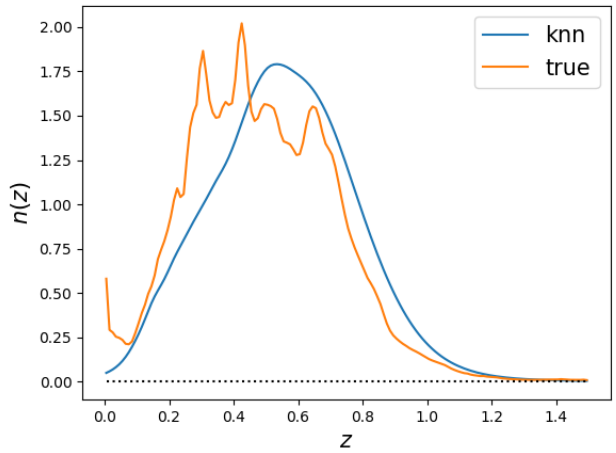


Figure 17. In this figure we show the redshift distribution $n(z)$ for the kNN photo-z (labelled as "knn") and the good redshift samples (labelled as "true"). In general, the two curves have similar scatter and very close amplitudes, demonstrating that the Gaussian scatter given by the kNN photo-z is applicable. However, significant disagreement is showing at $z \sim 0.4$, which corresponds to some redshift outlier problem in bin 2 of this work. We also notice that the kNN photo-z seems to be systematically higher.

Generally, the photo-z quality in this work is suitable for the study of self-calibration. The kNN photo-z (Zou et al. 2019) gives reliable best-fit photo-z and Gaussian scatter to present the underlying $n(z)$. However, we found that due to the redshift-color degeneracy discussed in Zou et al. (2019), there are some significant redshift outliers in our bin 2 and 3, which can lead to some bias in our w^{Gg} and w^{Ig}. This bias is smaller for red galaxies as their photo-z is generally better. There could also be biases due to training sample selection, for example Hartley et al. (2020), but they are beyond the scope of this paper.

B. CALCULATING THE LENSING-DROP AND IA-DROP Q

The lensing-drop Q^{Gg} and the IA-drop Q^{Ig} play crucial roles in lensing-IA separation (Eq. (8a) & (8b)), where $\{w^{Gg}, w^{Ig}\}$ comes from Hankel transformation as in Eq. (15). Therefore to get the Qs, we need to calculate the power spectra for $\{C^{Gg}, C^{Gg}|_S, C^{Ig}, C^{Ig}|_S\}$, with the given photo-z information of the survey.

Theoretically, C_{ii}^{Gg} is given by Eq. (11), and $C_{ii}^{Gg}|_S$ is given by

$$C_{ii}^{Gg}|_S(\ell) = \int_0^\infty \frac{W_i(\chi) n_i(\chi)}{\chi^2} b_g P_\delta \left(k = \frac{\ell}{\chi}; \chi\right) \eta_i^{Gg}(z) d\chi. \tag{B1}$$

The extra factor $\eta_i^{Gg}(z)$ arises from the fact that $C^{Gg}|_S$ only contains pairs with $z_\gamma^P < z_g^P$ (Zhang 2010a).

$$\begin{aligned} \eta_i^{Gg}(z) &= \eta_i^{Gg}(z_L = z_g = z) \ , \\ \eta_i^{Gg}(z_L, z_g) &= \frac{2 \int dz_G^P \int dz_g^P \int_0^\infty dz_G W_L(z_L, z_G) p(z_G|z_G^P) p(z_g|z_g^P) S(z_G^P, z_g^P) n_i^P(z_G^P) n_i^P(z_g^P)}{\int dz_G^P \int dz_g^P \int_0^\infty dz_G W_L(z_L, z_G) p(z_G|z_G^P) p(z_g|z_g^P) n_i^P(z_G^P) n_i^P(z_g^P)} \ . \end{aligned} \tag{B2}$$

Here z_L, z_g and z_G denote the lens redshift, the galaxy redshift, and the lensing source redshift, respectively. The quantities with superscript "P" denote photometric redshifts z^P and the ones without it are the true redshifts z. The integral $\int dz_G^P$ and $\int dz_g^P$ are both over $[z_{i,\min}^P, z_{i,\max}^P]$, namely the photo-z range of the i^{th} tomographic bin. The lensing kernel W_L for a flat universe is given by

$$W_L(z_L, z_S) = \begin{cases} \frac{3}{2}\Omega_m \frac{H_0^2}{c^2}(1+z_L)\chi_L(1-\frac{\chi_L}{\chi_S}) & \text{for } z_L < z_S \\ 0 & \text{otherwise} \end{cases} ; \tag{B3}$$

$p(z|z^P)$ is the redshift probability distribution function (PDF). In reality each galaxy has its own PDF. To speed up the calculation, we approximate it as a Gaussian function identical for all galaxies with the same z^P, as we adopted

in the previous work (Yao et al. 2017). $S(z_G^P, z_g^P)$ is the selection function for the "$|_S$" symbol,

$$S(z_G^P, z_g^P) = \begin{cases} 1 & \text{for } z_G^P < z_g^P \\ 0 & \text{otherwise .} \end{cases} ; \tag{B4}$$

$n_i^P(z^P)$ gives the photo-z distribution function in the $i^{\rm th}$ tomographic bin. The calculation of $\eta(z)$ can be extremely massive, since different galaxies (even with the same z^P) in general have different photo-z PDF. For fast calculation, we follow our previous work (Yao et al. 2017) and assume a uniform Gaussian PDF for all galaxies in the given photo-z bin,

$$p(z|z^P) = \frac{1}{\sqrt{2\pi}\sigma_z(1+z)} \exp\left\{ -\frac{(z - z^P - \Delta_z^i)^2}{2[\sigma_z(1+z)]^2} \right\} . \tag{B5}$$

σ_z in the above equation is the averaged photo-z scatter of all galaxies in the given photo-z bin. This assumption is valid because the redshift Gaussian scatter is tested in the machine learning method (Zou et al. 2019) and is also checked in Fig. 17 as they have similar height and scatter compared to the "true-z", despite of the outlier problem.

The factor 2 in Eq. (B3) arises from an integral equality theoretically predicted in Zhang (2010a),

$$\frac{\int_{z_{i,\rm min}^P}^{z_{i,\rm max}^P} dz_G^P \int_{z_{i,\rm min}^P}^{z_{i,\rm max}^P} dz_g^P n_i^P(z_G^P) n_i^P(z_g^P)}{\int_{z_{i,\rm min}^P}^{z_{i,\rm max}^P} dz_G^P \int_{z_{i,\rm min}^P}^{z_{i,\rm max}^P} dz_g^P n_i^P(z_G^P) n_i^P(z_g^P) S(z_G^P, z_g^P)} = 2 . \tag{B6}$$

This has also been tested numerically.

The Q^{Ig} introduce in this paper share similar definition as above. C_{ii}^{Ig} is defined in Eq. (13), while $C_{ii}^{Ig}|_S$ is defined as

$$C_{ii}^{Ig}|_S(\ell) = \int_0^\infty \frac{n_i(\chi) n_i(\chi)}{\chi^2} b_g P_{\delta,\gamma^I}\left(k = \frac{\ell}{\chi}; \chi\right) \eta_i^{Ig}(z) d\chi, \tag{B7}$$

in which η^{Ig} is given by

$$\eta_i^{Ig}(z_L, z_g) = \frac{2 \int dz_G^P \int dz_g^P \int_0^\infty dz_G p(z_G|z_G^P) p(z_g|z_g^P) S(z_G^P, z_g^P) n_i^P(z_G^P) n_i^P(z_g^P)}{\int dz_G^P \int dz_g^P \int_0^\infty dz_G p(z_G|z_G^P) p(z_g|z_g^P) n_i^P(z_G^P) n_i^P(z_g^P)}$$

simply without the lensing kernel $W_L(z_L, z_S)$ comparing to η^{Gg}, as the I-g correlation differs from the G-g correlation.

The calculation of $\{Q^{Gg}(\theta),\, Q^{Ig}(\theta)\}$ requires the photo-z distribution $n_i^P(z^P)$, the true redshift distribution $n_i(z)$, and cosmology (e.g. through P_δ and $W_L(z_L, z_S)$). However, its cosmological dependence is weak, since the cosmology dependent terms enter the same way in both C^{Gg} and $C^{Gg}|_S$ and therefore largely cancel each other in the ratio (Q). We tested for different cosmology in Table 1, the difference is at $\sim 10^{-3}$ to $\sim 10^{-5}$ level for Q. With the development in this paper, we also show the relation of power spectra based $Q(\ell)$ and correlation function based $Q(\theta)$ in Fig. 3 and 4.

C. POTENTIAL BIASES FROM SHEAR MEASUREMENTS AND REDSHIFT DISTRIBUTION

To further validate our results, we investigate the impact of (1) bias from shear calibration, and (2) bias from redshift distribution $n(z)$ calibration. We choose to use the red galaxies as an example, since its IA redshift-dependency $A_{\rm IA}(z)$ in Fig. 15 is the most delicate result of this work. We note accurate calibration in either shear (Pujol et al. 2020; Huff & Mandelbaum 2017; Sheldon & Huff 2017) or redshift (Hildebrandt et al. 2020b, 2017) are beyond the scope of this paper.

To have a better assessment on the impact of biased multiplicative bias m, we choose to cut off the "SIMP" type galaxies as in Phriksee et al. (2020). The shape measurements of "SIMP" subsample are quite noisy, so they contribute less in our results. Meanwhile by removing this type of galaxies, the remaining sample is dominated by the "EXP" type ($> 80\%$), whose multiplicative bias is accurately estimated as shown in Table A1 of Phriksee et al. (2020). We no longer use the default cut of $1 + m > 0.5$ as it could also introduce some selection bias. The associated results are shown in Fig. 18 with label "slt". Although the values of the IA amplitude $A_{\rm IA}$ changed slightly in each z-bin, we note by selecting different types of galaxies, the selected galaxies should have different IA amplitude. We emphasize that the

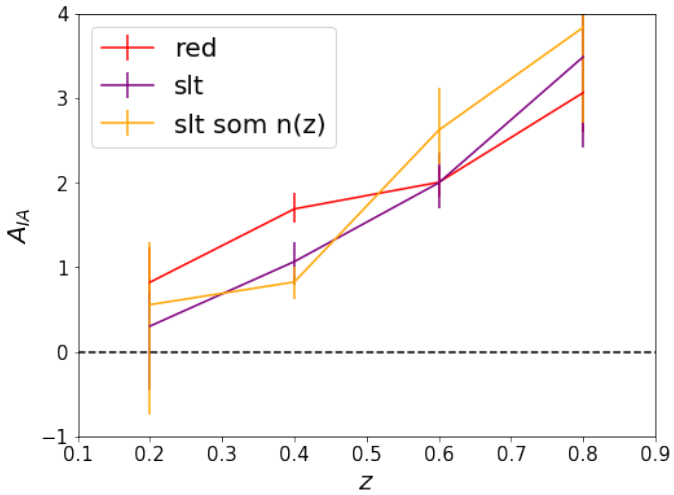


Figure 18. Test the $A_{\rm IA}(z)$ relation with the default cut (with "SIMP" galaxies and $1+m>0.5$) in red, with the selection for m-bias (without "SIMP" and without $1+m>0.5$) in purple, and impact from different $n(z)$ estimation in orange.

IA redshift-evolution result of the red galaxies remains the same: it rules out the constant IA amplitude assumption at $\sim 4\sigma$ (with slightly larger errorbars but reduced amplitude in the low-z bins, comparing with the default red sample).

We further address the impact of biased $n(z)$ estimation in the theoretical part. We match the "good photo-z catalog" described above (0.69M galaxies) with the "slt" red galaxy sample, resulting in 6.5k matches. Instead of using the $n(z)$ given by the kNN photo-z, we choose to use the distribution from the matched "good photo-z catalog" in the theoretical calculation of Eq. (11) and (13). In this way, the IA signal gives the orange "slt som n(z)"-labeled results in Fig. 18. Still, it shows the impact from the biased $n_i(z)$ is not significant, and the redshift-evolution result of the red galaxies remains the same. We note that getting $n(z)$ with another catalog will also add an extra selection bias on the IA amplitude.

Even though the above two tests on shear calibration and redshift distribution calibration are not required to produce the same results as our default red galaxy sample, they still agree at some level. Therefore we conclude that the $A_{\rm IA}(z)$ relation found for the red galaxies is robust against the described calibration biases.

D. COVARIANCE MATRIX FOR THE OBSERVABLES

We show the normalized covariance matrix of $\{w^{\gamma g}(\theta),\, w^{\gamma g}|_S(\theta)\}$ in Fig. 19. It is obvious that the two observables have a strong positive correlation, simply due to the fact that the data producing $w^{\gamma g}|_S(\theta)$ is completely included in $w^{\gamma g}(\theta)$. This positive correlation is converted into a negative correlation in the separated w^{Gg} and w^{Ig} (Fig. 6), through our lensing-IA separation method in Eq. (8a) and (8b). The only difference is the covariance of $\{w^{Gg}, w^{Ig}\}$ contains the statistical uncertainties from $\{Q^{Gg},\, Q^{Ig}\}$, which we tested to be at $\sim 10^{-3}$ level. So generally Fig. 6 and 19 carries equivalent information.

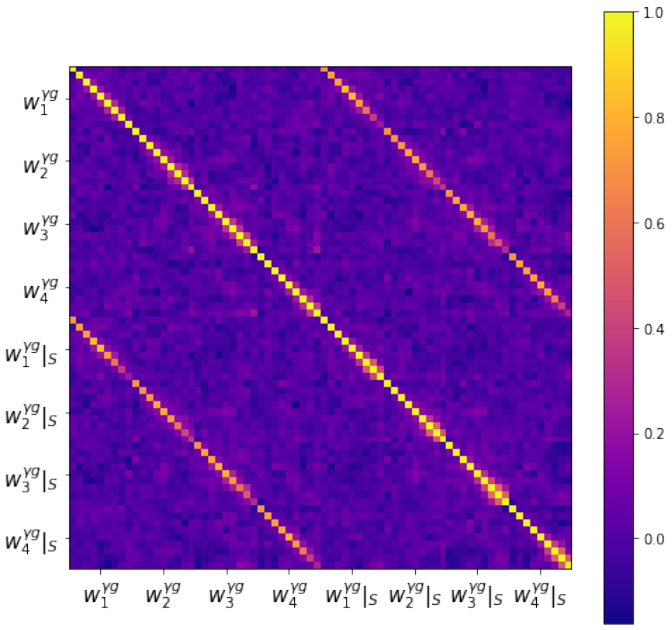


Figure 19. The normalized covariance matrix (the correlation coefficient $r_{ab} = Cov(a,b)/\sqrt{Cov(a,a)Cov(b,b)}$) for the LIS observable data vector $\{w^{\gamma g}(\theta),\ w^{\gamma g}|_S(\theta)\}$. There are 9 θ-bins for $w^{\gamma g}$ and 9 for $w^{\gamma g}|_S$, so the overall size for the data vector is 18 for each z-bin, leading to the 72×72 matrix for the full sample above. There are strong positive correlation between $w^{\gamma g}$ and $w^{\gamma g}|_S$, important for the data analysis.